Universidade do Minho
Escola de Ciências

Pedro Daniel Silva Chaves

Probing Dark Matter with Higgs Bosons and Top Quarks

Abril de 2023

Probing Dark Matter with Higgs Bosons and Top Quarks
Pedro Chaves
UMinho | 2023

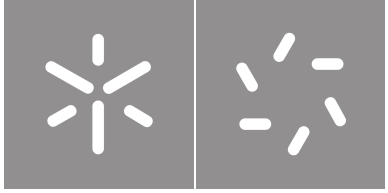

Universidade do Minho
School of Sciences

Pedro Daniel Silva Chaves

Probing Dark Matter with Higgs Bosons and Top Quarks

Master Thesis

Master in Physics

Work developed under the supervision of:
Professor Doutor António Joaquim Onofre de A. R. Gonçalves
Professor Doutor Rui Santos

April, 2023

This document was created with the (pdf/Xe/Lua)LaTeX processor and the NOVAthesis template (v6.9.15) [1].

Acknowledgements

I would like to thank everyone involved in the development of this work and supported me throughout this exciting journey. To my supervisor, Professor António Onofre, I would like to express my deepest thanks for all the tutoring, the guidance, the countless hours spent helping me fix software and code errors, the constructive criticism that kept me motivated and your insight on every topic that was approached in this project. Besides this, the good mood, the excitement, dedication and patience made this work really enjoyable. To Professor Rui Santos, my second supervisor, and to Duarte, thank you for the theoretical considerations that helped me learn on a more fundamental level this branch of Physics. To Rodrigo, I'm thankful for help in installing most of the tools I needed to develop this work in the very beginning. To João, thank you for all those meetings where we worked together and had fun times. My sincere thanks to all five for the friendship and great team spirit.

I would also like to thank my friends and colleagues for the support given throughout my academic path. My special thanks to Iga, for the good times we spent together, for always being present and cheering me up when I was feeling down and tired and for all the great discussions about science and life in general.

And finally, I'm extremely grateful to my mom and my brother for all the love and support given me for every decision I made so far and provided me with everything I needed to get where I am right now, both academically and personally.

STATEMENT OF INTEGRITY

I hereby declare having conducted this academic work with integrity. I confirm that I have not used plagiarism or any form of undue use of information or falsification of results along the process leading to its elaboration.

I further declare that I have fully acknowledged the Code of Ethical Conduct of the Universidade do Minho.

Abstract

Probing Dark Matter with Higgs Bosons and Top Quarks

The Dark Matter (DM) mystery, or, also called, the missing matter problem, is probably the most important astrophysical and cosmological problem to be solved in order to explain numerous phenomena that our current best theories of gravity fail to describe. These observations, gathered for the last century, imply the existence of extra matter in the Universe, to which we called dark matter, due to its non-interactive nature with the Standard Model (SM) interactions like the Electromagnetic (EM) force, making it extremely hard to detect. Although its existence is generally accepted, some astrophysicists argue for various modifications of the laws of general relativity, such as modified Newtonian dynamics, tensor-vector-scalar gravity, entropic gravity and some others. These models attempt to account for all observations without invoking supplemental matter. DM is thought to have had a strong influence on the structure and evolution of the Universe and to be non-baryonic, meaning it may be composed of some particles yet to be discovered, which constitutes another evidence supporting the incompleteness of the SM.

A phenomenological study is presented in this thesis in which a simplified DM model was used in order to perform the reconstruction of the $t\bar{t}$ system in the presence of a scalar dark matter particle, Y_0. In order to do this, signal samples of $pp \rightarrow t\bar{t}Y_0$ were generated at Leading Order (LO) using MadGraph5_aMC@NLO at the Large Hadron Collider (LHC), considering a pure CP-odd scalar boson, with a mass of m_{Y_0} = 0 GeV, and considering only the dileptonic final states of the top quark pair. An event analysis is described and applied to signal samples and background SM events, which are reconstructed using a kinematic fit, assuming all the contributions for the missing transverse energy belong only to the undetected neutrinos. Furthermore, CP angular observables, that were explored in the studies of the Higgs boson, were used to set Confidence Levels (CL) limits as a function of the CP nature of the top quark couplings to the proposed scalar particle Y_0. Of these observables, the $\Delta\phi_{\ell^+\ell^-}$ and b_4 variables were used to calculate exclusion limits for the CP-even and CP-odd components of the top quark DM couplings.

Keywords: Dark Matter, General Relativity, Standard Model

Resumo

O mistério da matéria escura é possivelmente o problema astrofísico e cosmológico mais significativo a ser resolvido pela comunidade científica a fim de explicar vários fenómenos que as melhores teorias da gravidade dos dias de hoje falham em descrever. As observações astronómicas realizadas no último século, implicam a existência de matéria extra no Universo, à qual chamamos matéria escura, devido à sua natureza não interactuante com as interações do Modelo Padrão, como é o caso da força eletromagnética, tornando a sua deteção particularmente difícil. Embora a sua existência seja geralmente aceite, existem modelos alternativos que envolvem possíveis alterações nas leis da relatividade geral, tais como a dinâmica modificada de Newton, gravidade tensorial-vetorial-escalar, gravidade entrópica, entre outras. Estes modelos tentam explicar todas as observações sem invocar matéria suplementar. Pensa-se que a matéria escura tenha tido uma forte influência na estrutura e evolução do Universo e de ser não-bariónica, ou seja, constituída por partículas que estão ainda por descobrir, dando assim mais uma indicação de que o Modelo Padrão está de facto incompleto.

Nesta dissertação é apresentado um estudo fenomenológico no qual foi utilizado um modelo de matéria escura simplificado que considera a produção de um sistema $t\bar{t}$ associado a uma partícula escalar de matéria escura, Y_0. Para este objetivo, amostras de sinal do tipo $pp \longrightarrow t\bar{t}Y_0$ foram geradas à ordem mais baixa (LO) usando o gerador Monte Carlo MadGraph5_aMC@NLO no LHC (Large Hadron Collider), considerando um bosão puramente CP-ímpar, com uma massa de m_{Y_0} = 0 GeV, e considerando apenas estados finais dileptónicos. A análise descrita foi efetuada nestas amostras de sinal em conjunto com eventos de fundo do Modelo Padrão e estes foram reconstruídos com recurso a um ajuste cinemático, assumindo que toda a energia transversa em falta pertence aos neutrinos, provenientes dos decaimentos do quark top e que não são detetados. Para além disto, observáveis angulares, que foram explorados anteriormente em estudos do bosão de Higgs, foram usados para definir limites nos níveis de confiança com que se detetam estas partículas em função da natureza CP dos acoplamentos do quark top à partícula proposta Y_0. Destes observáveis, houve um particular foco na diferença do ângulo azimutal dos dois leptões presentes nos eventos ($\Delta\phi_{\ell^+\ell^-}$) e na variável b_4 para calcular limites de exclusão aos acoplamentos do quark top ao mediador de matéria escura.

Palavras-chave: Matéria escura, Relatividade Geral, Modelo Padrão

Contents

List of Figures

List of Tables

Acronyms

2D PDF Two-dimensional Probability Density Function *(p. 40)*

BDTG Boosted Decision Tree with a Gradient Boost *(pp. xi, 38, 40)*
BSM Beyond the Standard Model *(pp. 7, 28)*

CDM Cold Dark Matter *(pp. 14, 15)*
CL Confidence Levels *(pp. v, xi, 46–50)*
CMB Cosmic Background Microwave *(pp. 11, 12, 14)*
CSC Cathode Strip Chambers *(p. 24)*

DM Dark Matter *(pp. v, xi, xii, 1, 2, 10–17, 28, 34, 37, 39, 41, 44, 46–50)*

ECAL Electromagnetic Calorimeter *(pp. 30–32, 36)*
ECO Exotic Compact Object *(p. 2)*
EM Electromagnetic *(pp. v, 10, 22, 23, 26, 28)*

FCal Forward Calorimeter *(p. 23)*

GR General Relativity *(pp. 1, 12, 14)*

HCAL Hadronic Calorimeter *(pp. 30, 36)*
HEP High Energy Physics *(p. 2)*
HL-LHC High-Luminosity LHC *(pp. x, 18, 19, 46, 49)*

ID Inner Detector *(pp. 20, 21, 24, 26–28)*
IP Interaction Point *(pp. xi, 19, 21, 23–25, 27)*

L1 Level-1 *(pp. 25, 26)*
L2 Level-2 *(pp. 25, 26)*
LAB Laboratory Frame *(pp. 44, 48)*
LAr Liquid-Argon *(pp. x, 20, 22, 23, 28)*
LHC Large Hadron Collider *(pp. v, x, xii, 2, 8, 15, 17–19, 27, 29, 31, 34, 35, 44, 46, 49)*
LO Leading Order *(pp. v, xi, 34, 35)*

MACHOs MAssive Compact Halo Objects *(pp. 12, 13, 15)*
MC Monte Carlo *(p. 37)*
MDT Monitored Drift Tube *(p. 24)*
MET Missing Transverse Energy *(p. 28)*
MOND Modified Newtonian Dynamics *(pp. 12, 14)*
MSSM Minimal Supersymmetric Standard Model *(p. 15)*

NLO Next-to-Leading Order *(p. 35)*
NNLL Next-to-Next-Leading Logarithmic *(pp. x, 8, 35)*
NNLO Next-to-Next-Leading Order *(pp. x, 8, 35)*

PBHs Primordial Black Holes *(p. 15)*

QCD Quantum Chromodynamics *(pp. x, 6, 8, 14, 19, 35)*
QFT Quantum Field Theory *(p. 1)*

ROC Reciever Operating Characteristic *(pp. xi, 38, 40)*
RoI Region of Interest *(p. 26)*
RPC Resistive Plate Chambers *(p. 24)*

SCT Semiconductor Tracker *(p. 21)*
SM Standard Model *(pp. v, xi, xii, 1–8, 14–16, 19, 29, 35, 45–49)*
SUSY Supersymmetry *(pp. 14, 28)*

TeVeS Tensor-Vector-Scalar Gravity *(p. 14)*
TGC Thin Gap Chambers *(p. 24)*
TileCal Tile Calorimeter *(p. 23)*
TMVA Toolkit for Multivariate Analysis *(pp. xi, 38, 39, 41)*
TRT Transition Radiation Tracker *(pp. 21, 24)*

WIMPS Weakly Interacting Massive Particles *(p. 14)*

ZDC Zero-Degree Calorimeter *(p. 25)*

1

Introduction

The 20th century was the pinnacle time in which the development of modern physics took place. Followed by Einstein's General Relativity (GR) [2], we had another revolution in the physics world - quantum mechanics (1920s). This completely new branch was the foundation for creating the technology we have today. It was also the pillar that allowed us to describe interactions between the building blocks of matter - particles. Interactions that, if put together in a single model of physics, can describe everything that is around us. And that is what Quantum Field Theory (QFT) did in the years that followed. Following the discovery of two new interactions - the strong nuclear force and the weak nuclear force - QFT allowed us to build this model that contains three of the four interactions in Nature: the electromagnetic, strong and weak nuclear forces (gravity remains to be included). This model was developed in the latter half of the 20th century through the work of several authors worldwide [3], with the current formulation being finalized in the mid-1970s after the experimental confirmation of the existence of quarks. This quantum framework is called the SM of particle physics [4–6].

The SM is currently the best description we have of our understanding of particle physics where the forces between particles are mediated by the exchange of additional particles, named the gauge bosons. The model explains the mechanism through which elementary particles acquire mass, it successfully predicted the weak neutral currents [7] (which led to the discovery of the W and Z bosons) and describes a large number of particles that have already been discovered, the last one being the Higgs boson.

Although it provides a successful picture of all current experimental data, the SM is incomplete. There are a lot of questions that remain unanswered. It can't explain why particles have the mass they have [8], it doesn't explain the observed matter-antimatter asymmetry of the Universe [9], it doesn't contain a DM candidate (which will be approached in this thesis), it considers neutrinos are massless, even though we observed oscillations between flavours [10–12], thus proving they do have mass, and it doesn't incorporate the gravity interaction as described by the . Given the number and importance of the open questions, extensions to the SM are of utmost importance to explore possible answers and tests to these questions.

As previously mentioned, the SM doesn't provide a viable candidate for a DM particle. Although various astrophysical and cosmological observations provide strong hints for the existence of DM, very

little is known about its true nature. Constraints on models from various direct/indirect detection experiments and from cosmology still allow for a wide range of DM masses and couplings to the SM particles. Nonetheless, we can build extensions of the SM to include this kind of elementary particle. In order to motivate this, many different models have been proposed. Recently, an alternative interpretation of the signal GW190521, detected in the LIGO-Virgo Collaboration [13], has been proposed as being a merger of two Proca Stars, which is a possible Exotic Compact Object (ECO) composed by new bosons. Confirmation of this Proca Star interpretation would provide the first evidence for a DM particle, in this case, a new boson with mass ($8.7\times10^{-13}\pm 1\times10^{-13}$) eV [14]. The objective of this thesis is therefore to explore extensions of the SM that will add a new boson - in our case, a spin-0 boson - of very small mass and will be considered a DM mediator candidate. The approach will be to use a simplified DM model [15] and generate events of the type $pp \rightarrow t\bar{t}Y_0$, where Y_0 is the spin-0 DM mediator the model proposes which interacts weakly with the SM matter. We will consider the dileptonic decay of the top quarks as the final state ($t\bar{t} \rightarrow b\bar{b}W^+W^- \rightarrow b\bar{b}\nu\bar{\nu}\ell^+\ell^-$), where ℓ denotes either an electron or a muon. We will also focus on the reconstruction of the $t\bar{t}$ system and as the final step we will compare the distributions obtained with SM-like events.

The structure of this thesis is then the following: in Chapter 1 we will go through a brief revision of the SM. The top quark is also discussed, some of its properties and its importance for experimental observations in High Energy Physics (HEP). And lastly, we will talk about Dark Matter, what we think it could be, how we know it exists and some models that have been proposed to try predicting the existence of these particles and how they could interact with particles of the SM (including the model used in this work). In Chapter 2, the experimental setup, in which the observation of these hypothetical particles can take place, is described. We'll talk briefly about the LHC [16] and one of its main detectors, ATLAS [17]. However, since this work is based on fast simulated events, we used DELPHES [18] for simulating this detector, which will also be described. The full description of the signal and background generation, event selection and reconstruction of the $t\bar{t}$ system is given in Chapter 3. In our reconstruction, we included truth-matching methods, which were used to match the corresponding reconstructed objects to the generated particles. In Chapter 4, our results are presented, including the angular distributions and the evaluation of the exclusion limits on the discrimination of the SM plus a new CP-odd particle (our DM candidate) with respect to the SM only hypothesis. A summary is given in Chapter 5.

1.1 The Standard Model of Particle Physics

The Standard Model of Particle Physics, or just SM, is the theory that explains how particles interact with each other through three of the four known fundamental forces (electromagnetic, weak and strong interactions), gravity being excluded. We know matter is composed by atoms and atoms are composed by protons, neutrons and electrons. However, when we look at higher energy scales, we can observe a much richer structure. We see that protons and neutrons are bound states of elementary particles, called quarks. Besides quarks, which experience the four fundamental interactions, we discovered another family of elementary particles, called leptons. The leptons do not interact via the strong force and they can either be charged, like the electron, or neutral (neutrinos). These two subsets of particles form a set within the SM called fermions.

Fermions are particles that obey Fermi-Dirac statistics, having half-integer spin (so far we discovered spin-$1/2$ particles) and obey the Pauli exclusion principle. In total there are six quarks and six leptons, each having their own antiparticle, and they are organized in three generations. Each generation has a quark pair and a lepton pair and each one is a copy of the other but with different masses (see Figure 1). A mass hierarchy is observed within the generations, the third one containing heavier quarks and leptons than the second generation, and the second containing heavier quarks and leptons than the first, and this is something the SM cannot yet explain. The interactions between these elementary particles are mediated by spin-1 particles, called gauge or vector bosons. In contrast to fermions, which are the constituents of matter, these bosons act as force carriers. For example, the force carrier of the electromagnetic force, is the photon (γ), which is neutrally charged and massless, and it interacts with all charged particles. For the strong force we have the gluons mediating the interaction, which are also massless and they carry color charge and interact with all particles carrying color charge (quarks and gluons themselves). The weak interaction is mediated by the Z (neutrally charged), W^+ and W^- (charge $\pm|e|$) bosons.

Finally, the Higgs boson is electrically neutral and has spin 0, making it the only fundamental scalar particle in the SM discovered so far. This boson does not play the role of a force carrier. It has a special role in the SM, since it provides the mechanism by which all other fundamental particles acquire mass (Higgs mechanism).

1.2 Some theoretical considerations behind the SM

Formally, the SM is a mathematical construct based on a gauged quantum field theory, where the dynamics and kinematics of the theory are dictated by a Lorentz invariant Lagrangian density (or just, Lagrangian) which contains the internal symmetries of the unitary product group $SU(3)_C \times SU(2)_L \times U(1)_Y$. The $SU(3)_C$ group includes the symmetry of the strong interactions and it has eight gauge fields, $G^{\alpha}_{\mu}(\alpha = 1, ..., 8)$, one for each of the eight gluons that exists. The $SU(2)_L$ group contains the symmetry of the weak interactions and it has 3 gauge fields, $W^i_{\mu}(i = 1, 2, 3)$, and the group $U(1)_Y$ has one gauge field usually denoted by B_{μ}. We can talk about the product of the last two groups, $SU(2)_L \times U(1)_Y$,

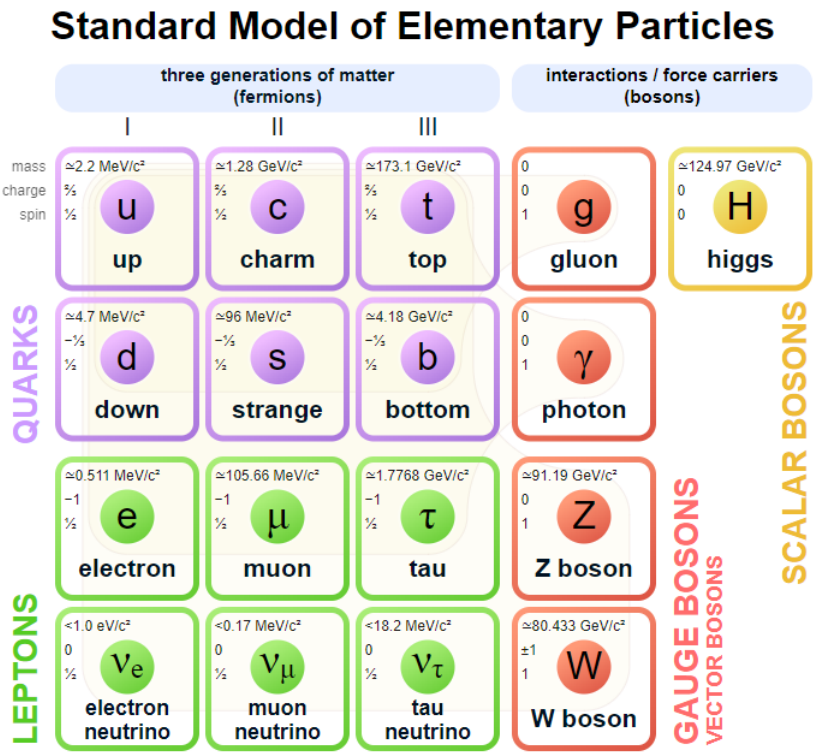

Figure 1: Elementary particles of the Standard Model, with the three generations of quarks and leptons (the mass hierarchy in the fermionic generations is visible) [19].

as one entity since we have been able to unify the electromagnetic interaction with the weak interaction into what we call the electroweak interaction. It is through the spontaneous symmetry breaking of the electroweak symmetry $SU(2) \times U(1)_Y$, which is a result of the Higgs mechanism, that the physically observed states, associated to the W_μ^i and B_μ fields, are produced. The W^1 and W^2 fields combine to produce the $W^\pm$ bosons and the W^3 and B_μ fields mix to produce the Z boson and the photon. And so, by describing all the particles and all these interactions between them, we can write the SM lagrangian as

$$\mathcal{L}_{SM} = \mathcal{L}_{Gauge} + \mathcal{L}_{Fermion} + \mathcal{L}_{Higgs} + \mathcal{L}_{Yukawa} \tag{1.1}$$

The first term, $\mathcal{L}_{Gauge}$, takes into account the kinematic and self interacting terms of the gauge fields and we can write it as:

$$\mathcal{L}_{Gauge} = -\frac{1}{4}B_{\mu\nu}B^{\mu\nu} - \frac{1}{4}W^i_{\mu\nu}W^{i\mu\nu} - \frac{1}{4}G^\alpha_{\mu\nu}G^{\alpha\mu\nu} \tag{1.2}$$

And for these spin-1 fields, this Lagrangian is written in terms of the field strength tensors

$$B_{\mu\nu} = \partial_\mu B_\nu - \partial_\nu B_\mu \quad , \tag{1.3}$$

$$W^i_{\mu\nu} = \partial_\mu W^i_\nu - \partial_\nu W^i_\mu + g_w \epsilon^{ijk} W_{j\mu} W_{k\nu} \quad , \tag{1.4}$$

$$G^{\alpha}_{\mu\nu} = \partial_{\mu}G^{\alpha}_{\nu} - \partial_{\nu}G^{\alpha}_{\mu} + g_s f^{\alpha\beta\gamma}G_{\mu\beta}G_{\nu\gamma} \quad , \tag{1.5}$$

where g_s and g_w are the coupling constants of each gauge field (the first equation doesn't have a coupling term, because photons don't interact with themselves) and ϵ^{ijk} and $f^{\alpha\beta\gamma}$ are the structure constants of the particular gauge group and they are necessary to specify the form for the Lie algebra of the groups in order to preserve the gauge invariance whenever the generators of the respective group do not commute.

The term $\mathcal{L}_{Fermion}$ describes how fermions couple to the gauge fields (bosons). But to understand this a bit more intuitively, we first need to talk about the chirality of a particle as well as the weak isospin, weak hypercharge and color charge quantum numbers.

Chirality is a Lorentz invariant and is an intrinsic property of a particle, like mass, charge or spin. By definition we say that fermions can be left-chiral or right-chiral and we can write the wavefunction for a fermion as the sum of these two states

$$\Psi = \Psi_R + \Psi_L \quad , \tag{1.6}$$

where each of these states is obtained by projection operators acting on a spinor. These projection operators are defined as

$$P_R = \frac{\mathbb{1} + \gamma^5}{2} \qquad\qquad P_L = \frac{\mathbb{1} - \gamma^5}{2} \quad , \tag{1.7}$$

where γ^5 is the matrix defined by the product of the Dirac matrices

$$\gamma^5 = i\gamma^0\gamma^1\gamma^2\gamma^3 \quad , \tag{1.8}$$

having eigenvalues ± 1. Fermions are called right-handed (R) if they have chirality +1, and left-handed (L) if they have chirality -1. The concept of chirality is important for the SM because it was discovered, unlike the strong and electromagnetic interactions, that the weak interaction is not chiral symmetric.

The interaction between the fermions and the gauge bosons in obtained using the $SU(2) \times U(1)$ gauge group as will be described below. The gauge group $U(1)$ has only one generator - the hypercharge - with a coupling constant g'. The $SU(2)$ gauge has three generators given by the weak isospin operator $\hat{T} = \sigma_i/2$, with σ_i being the Pauli matrices

$$\sigma_1 = \begin{pmatrix} 0 & 1 \\ 1 & 0 \end{pmatrix}, \quad \sigma_2 = \begin{pmatrix} 0 & -i \\ i & 0 \end{pmatrix}, \quad \sigma_3 = \begin{pmatrix} 1 & 0 \\ 0 & -1 \end{pmatrix} \quad , \tag{1.9}$$

with a coupling constant g_w. The weak isospin and weak hypercharge quantum numbers are related to the electric charge by the Gell-Mann-Nishijima formula

$$Q = T_3 + \frac{Y}{2} \quad , \tag{1.10}$$

where T_3 is the third component of the weak isospin quantum number. It is also noteworthy that for left-handed particles we have $T_3 = \pm 1/2$, and for right-handed particles we have $T_3 = 0$. We can then

group left-handed fermions into $SU(2)$ doublets that behave the same way under the weak interaction

$$\begin{pmatrix} u_L \\ d_L \end{pmatrix}, \quad \begin{pmatrix} c_L \\ s_L \end{pmatrix}, \quad \begin{pmatrix} t_L \\ b_L \end{pmatrix}, \quad \begin{pmatrix} e_L \\ \nu_{e_L} \end{pmatrix}, \quad \begin{pmatrix} \nu_L \\ \nu_{\mu_L} \end{pmatrix}, \quad \begin{pmatrix} \tau_L \\ \mu_{\tau_L} \end{pmatrix} \tag{1.11}$$

where u_L, c_L and t_L are the up-type quarks, with $T_3 = 1/2$, d_L, s_L and b_L are the down-type quarks, with $T_3 = -1/2$, e_L, μ_L and τ_L are the electrons, muons and taus, respectively with $T_3 = -1/2$ and ν_{e_L}, ν_{μ_L} and ν_{τ_L} are the neutrinos, with $T_3 = 1/2$. Right-handed particles are singlets of $SU(2)$ ($T_3 = 0$).

The interaction between the fermions and the gluons is described by QCD, which is a non-abelian gauge theory with the gauge group $SU(3)$ [20]. It describes the interactions between coloured particles, where colour is a quantum number. Only quarks (and anti-quarks) have colour charge, thus being the only ones that interact with the gluon fields G_μ^α. The $SU(3)$ group has eight generators that represent each of the eight gluons and are written as

$$t_a = \frac{\lambda_a}{2} \quad , \tag{1.12}$$

where λ_a (a = 1,2,...,8) are the Gell-Mann matrices

$$\lambda_1 = \begin{pmatrix} 0 & 1 & 0 \\ 1 & 0 & 0 \\ 0 & 0 & 0 \end{pmatrix}, \quad \lambda_2 = \begin{pmatrix} 0 & -i & 0 \\ i & 0 & 0 \\ 0 & 0 & 0 \end{pmatrix}, \quad \lambda_3 = \begin{pmatrix} 1 & 0 & 0 \\ 0 & 1 & 0 \\ 0 & 0 & 0 \end{pmatrix}, \quad \lambda_4 = \begin{pmatrix} 0 & 0 & 1 \\ 0 & 0 & 0 \\ 1 & 0 & 0 \end{pmatrix}, \tag{1.13}$$

$$\lambda_5 = \begin{pmatrix} 0 & 0 & -i \\ 0 & 0 & 0 \\ i & 0 & 0 \end{pmatrix}, \quad \lambda_6 = \begin{pmatrix} 0 & 0 & 0 \\ 0 & 0 & 1 \\ 0 & 1 & 0 \end{pmatrix}, \quad \lambda_7 = \begin{pmatrix} 0 & 0 & 0 \\ 0 & 0 & -i \\ 0 & i & 0 \end{pmatrix}, \quad \lambda_8 = \frac{1}{\sqrt{3}} \begin{pmatrix} 1 & 0 & 0 \\ 0 & 1 & 0 \\ 0 & 0 & -2 \end{pmatrix}$$

With all of this in mind, we can now write the second term of the SM lagrangian as

$$\begin{aligned} \mathcal{L}_{Fermion} = & \sum_{i=1}^{3} i\overline{Q}_{L_i}\gamma^\mu \left(\partial_\mu - ig'\frac{Y}{2}B_\mu - i\frac{g_w}{2}\sigma_i W_\mu^i - i\frac{g_s}{2}\lambda_\alpha G_\mu^\alpha\right) Q_{L_i} \\ & + \sum_{i=1}^{3} i\overline{Q}_{R_i}\gamma^\mu \left(\partial_\mu - g'\frac{Y}{2}B_\mu - \frac{g_s}{2}\lambda_\alpha G_\mu^\alpha\right) Q_{R_i} \\ & + \sum_{j=1}^{3} i\overline{L}_{L_j}\gamma^\mu \left(\partial_\mu - g'\frac{Y}{2}B_\mu - \frac{g_w}{2}\sigma_i W_\mu^i\right) L_{L_j} \\ & + \sum_{j=1}^{3} i\overline{l}_{R_j}\gamma^\mu \left(\partial_\mu - g'\frac{Y}{2}B_\mu\right) l_{R_j} \quad , \end{aligned} \tag{1.14}$$

where the indexes i and j refer to the generations of families of the quarks and leptons, respectively, and the following sets were defined:

$$\begin{aligned} & Q_L = \{(u_L, d_L), (c_L, s_L), (t_L, b_L)\}, \qquad Q_R = \{u_R, d_R, c_R, s_R, t_R, b_R\} \\ & L_L = \{(e_L, \nu_{e_L})\}, (\mu_L, \nu_{\mu_L}), (\tau_L, \nu_{\tau_L})\}, \qquad l_R = \{e_R, \mu_R, \tau_R\} \end{aligned} \tag{1.15}$$

and D_μ is the covariant derivative defined as:

$$D_\mu = \partial_\mu - ig'\frac{Y}{2}B_\mu - i\frac{g_w}{2}\sigma_i W_\mu^i - i\frac{g_s}{2}\lambda_\alpha G_\mu^\alpha \tag{1.16}$$

The first term in equation 1.14 corresponds to the interaction of the left-handed quarks (and anti-quarks) to the gauge fields; the second term corresponds to the interaction of the right-handed quarks to the electromagnetic and strong forces; the third term describes the interactions of left-handed leptons to the electromagnetic and weak forces; and the last term corresponds to the right-handed leptons and their interaction with the electromagnetic fields.

Very briefly, $\mathcal{L}_{Higgs}$ describes how the force carrying particles interact with the Higgs field and represents how the weak force carrying particles acquire their mass. It can be written as

$$\mathcal{L}_{Higgs} = (D_\mu\phi)^\dagger D^\mu\phi + \mu^2\phi^\dagger\phi - \lambda(\phi^\dagger\phi)^2 \quad , \tag{1.17}$$

where ϕ is the Higgs field and $\lambda > 0$ and $\mu^2 < 0$, so that the mechanism of spontaneous symmetry breaking can be used. The last two terms are usually written as $V(\phi)$, which is called the Higgs potential and it describes how the Higgs boson interacts with itself.

And finally, $\mathcal{L}_{Yukawa}$ is the lagrangian that gives the mass to all fermions. It can be written as

$$\mathcal{L}_{Yukawa} = -(K_1\overline{\Psi}_L\phi\Psi_R + K_2\overline{\Psi}_R\tilde{\phi}\Psi_L + h.c.) \quad , \tag{1.18}$$

where $\tilde{\phi} = iT_2\phi^*$. The couplings K_1 and K_2 are chosen, such that, after electroweak symmetry breaking, this will give a mass term to all the fermions.

We have just scratched the surface of the theoretical framework behind the SM. It has proven to be one of the most successful theories to date, if not the most successful. However, like it was said previously, it is still incomplete. We keep trying to add extensions to this theory to address some of the major problems and mysteries we encounter. We say these models explore physics Beyond the Standard Model (BSM). These and others require a higher energy scale to discover new particles, new symmetries, new dimensions and perhaps something more.

1.3 Top Quark

Predicted in 1977 by Makoto Kobayashi and Toshihide Maskawa to explain the observed CP violations in kaon decay [21], the top quark was discovered in 1995 by the CDF and DØ experiments at Fermilab [22, 23] with a reported mass of m_t = 176 ± 8 (stat.) ± 10 (sys.) GeV/c^2 and, as it was predicted by the SM, its charge is $+2/3|e|$. It's the heaviest elementary particle (with Yukawa coupling being almost equal to 1), it was the last discovered quark and, together with the bottom quark, completes the third generation of fermions. As of 2022, the latest Tevatron average gives a value of m_t = 174.30 ± 0.35 (stat.) ± 0.54 (sys.) GeV/c^2 [24] and with new statistical and experimental methods, the CMS collaboration reported their most precise measurement from the data sample collected on 2016, m_t = 171.77 ± 0.04 (stat.) ± 0.38 (sys.) GeV/c^2 [25]. The ATLAS collaboration also reported this year a new result for the top quark mass, m_t = 174.41 ± 0.39 (stat.) ± 0.66 (sys.) GeV/c^2 [26], using the datasets obtained in 2015 and 2016. Figure 2 shows top quark pair production cross section as a function of the center-of-mass energy from Tevatron and LHC.

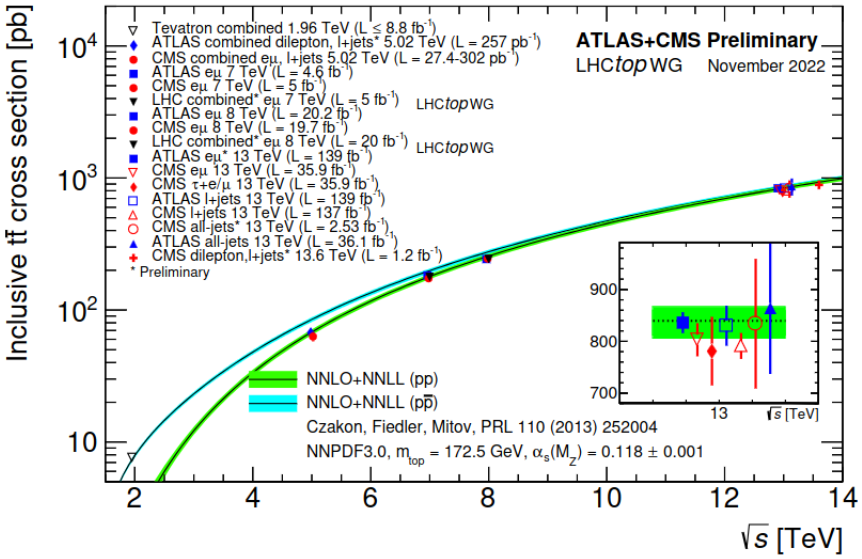

Figure 2: Summary of LHC and Tevatron measurements of the top-pair production cross-section as a function of the centre-of-mass energy compared to the NNLO QCD calculation complemented with NNLL resummation (top++2.0). The measurements and the theory calculation are quoted at m_t = 172.5 GeV [27].

It's of paramount importance to get precise knowledge of the properties of this particle since the top-quark's mass is a free parameter of the SM and it significantly affects the quantum corrections to both the Higgs boson and W boson masses, thus providing a relationship that can be used for precision tests and consistency of the SM. Moreover, a precise measurement of the top-quark's mass is required to predict the evolution of the Higgs quartic coupling at high scales and predicting with more certainty the stability of our Universe.

The decay width of the top quark has been measured by the various experiments mentioned just above being in the interval 1.36 GeV $< \Gamma_t <$ 2.00 GeV. With these decay widths, we can estimate the

mean lifetime of the top quark, through the Heisenberg's uncertainty principle, being in the range of approximately 3.29×10^{-25} s < τ_t < 4.84×10^{-25} s , which is about a twentieth of the timescale for strong interactions and, therefore, it decays to other particles instead of forming hadrons, contrary to the other quarks. This gives an opportunity to study the behaviour of a "bare" quark, which transfers its quantum numbers such as spin information directly to the final state decay products. This, consequently, enables the measurement of the top quark's polarization. Even though top-antitop pairs are unpolarized when produced in particle colliders, their spins are very strongly correlated [28] and have been explored as a probe of new physics through the measurement of angular distributions.

The main decay channel is through the weak interaction producing a W boson and a bottom quark ($t \rightarrow W^+b$ and $\bar{t} \rightarrow W^-\bar{b}$) with a probability very close to unity. Since the W boson has multiple channels to which it can decay, we can classify the top quark decay based on these channels: it is called leptonic decay if the W decays into a lepton and a neutrino, with a probability of approximately 33.2%, and hadronic if the W decays to a quark and anti-quark pair, being more likely to happen with a probability of 66.5% [24].

1.4 Dark Matter

Known as one of the biggest unsolved mysteries in Particle Physics, Astrophysics and Cosmology, DM is a hypothetical form of matter thought to account for approximately 85% of the matter in the Universe. In this section, most of all the evidence for the existence of DM is given and how the scientific community, throughout a century of studies and experimental observations, implied the existence of this unknown matter that does not interact with the EM field, making it extremely difficult to detect. Among these observations are the effects of gravitational lensing, the velocity curves of galaxies and mass location during galaxy clusters collisions.

Various hypothesis to solve this major problem are also exposed in this section, including modified theories of gravity and the existence of new particles. Experimental methods to try to detect such particles are also briefly described. A description of simplified models is also given, including the one used in this work, and how we use them to restrict some of the free parameters of interest.

1.4.1 Historical background

The first person to ever conceive the idea of DM was Lord Kelvin in 1884 when he was trying to measure the velocity of the stars in the Milky Way galaxy and he was doing this to check if the stars were in a stable system. In other words, he wanted to see if the kinetic energy of the stars was equal to the gravitational energy they had. And so, with the measurements of the observed velocity dispersion, which is proportional to the mass of the system, of the stars orbiting around the galaxy, he estimated the mass of the galaxy to be larger than the mass of the visible stars. Therefore he concluded that, out of the many stars in the galaxy, the majority of them should be "dark bodies" [29]. However, this idea wasn't well accepted by Henry Poincaré, who was the first to call this mysterious substance "Dark Matter" [30], since the number Kelvin obtained was comparable to that which the telescopes gave.

However, in the 1930s, things started to get more interesting. In 1930, Knut Lundmark compared the mass we calculate to be in a galaxy and the mass suggested by the light received - the mass to light ratio (M/L) - and he measured this for five new galaxies that were discovered back then. For this sample, this ratio was between 6 and 100, thus pointing to the conclusion that indeed something else exists [31]. In 1933 Fritz Zwicky measured the velocity dispersion, only this time for the Coma galaxy cluster and obtained a M/L of about 400 [32, 33]. Besides this, he also estimated that those 800 galaxies had a velocity of 1000 km/s, instead of the predicted 80 km/s. These values were proven to be off by a factor of 8, due to the fact that we didn't know how quickly the Universe was expanding, however he correctly concluded the bulk of the matter was indeed "dark". In 1939, the astronomer Horace Babcock published his PhD thesis in which he measured the rotation curve of the Andromeda galaxy (M31) [34], meaning that he measured how fast stars were rotating around the center of the galaxy at increasing radius. Since we see more stars in the center of galaxies, it was expected this rotation velocity would decrease with distance, like the case of our Solar System where the outer planets have slower velocities. However Babcock found the exact

opposite result, suggesting there is more mass in the outskirts of the galaxy than in the center. Figure 3 shows the results obtained by observations of the rotation curves of the galaxies M31, by Babcock, and the M81 and M101 galaxies later researched (1970s) by Morton Roberts and Arnold Rots, showing that velocity does not decrease with distance.

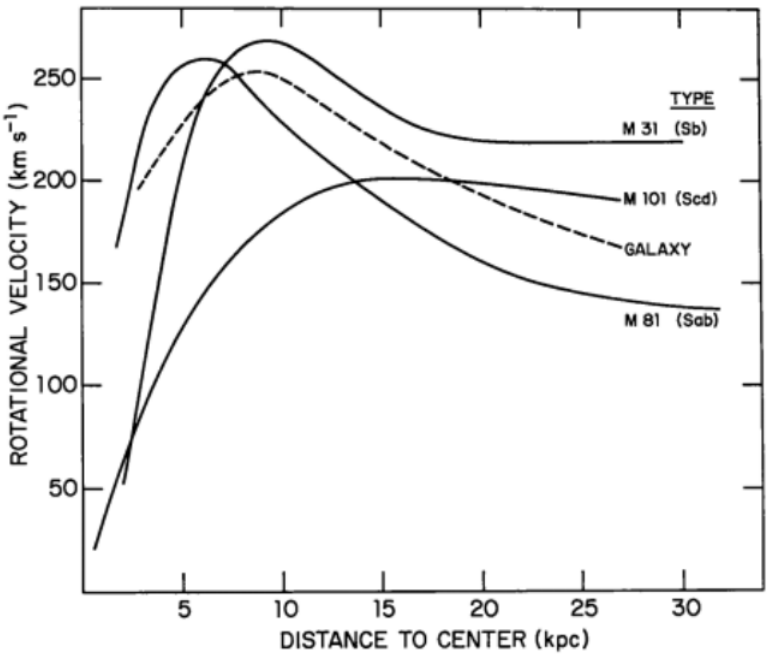

Figure 3: The rotation curves for the galaxies M31 (Andromeda galaxy), M81 (Bode's galaxy) and M101 (Pinwheel galaxy) (solid lines) obtained by Roberts and Rots in 1973. The dashed curve, obtained from Babcock is represented for comparison [35].

As cosmology matured as a science with the discovery of the Cosmic Background Microwave (CMB) [36], in 1965, and the acknowledgment that the Universe had a beginning, scientists began to wonder what would the end of the Universe would be. So, they realized it depended on the balance between gravity pulling all the matter in the Universe together and the expansion (also already acknowledged) pushing matter outwards, making critical the measurement of how much matter there is in the Universe, in order to understand if we are going to have a collapsing Universe ("Big Crunch"), an expanding one or if we are going to have an equilibrium state. It was from this point this "missing matter problem" stopped being just a curiosity and started being treated as a major unsolved problem in cosmology and astronomy until today.

Through the majority of the 1960s, most scientists thought this missing matter was gas that was in between the galaxies (within the clusters) and we couldn't see it. Although by the end of the decade we actually managed to detect this hot gas, but it could only account for 10% (in some cases only 2%) for the gravitational mass of the respective cluster.

In the 1970s and 1980s, research and observations related to DM started to become more common. More rotation curves were being plotted for different galaxies and clusters and all revealed the same

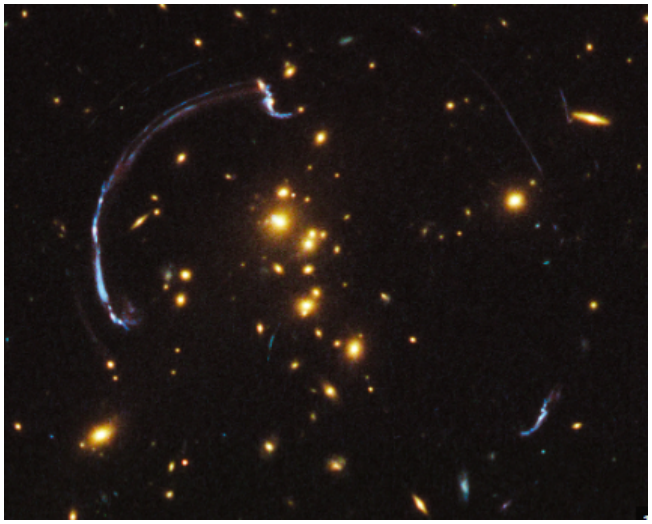

Figure 4: Galaxy cluster RCS2 032727-132623. This picture shows a distant galaxy 10 billion light-years away as it appears through the gravitational lens around the galaxy cluster RCS2 032727-132623 about 5 billion light-years away.

behaviour: the velocity on the outskirts was flat, instead of decreasing. Therefore, it was concluded that the observed visible mass of a galaxy did not have enough gravity to hold these fast-moving stars together, reporting thus the existence of a dark "halo" surrounding each galaxy. Later, in 1979, the astronomers Dennis Walsh, Bob Carswell and Ray Weymann observed the first "twin quasars" [37], but they noticed they were separated only by 0.0016°, their brightness was roughly the same, their spectra had the almost the same exact shape and their redshift was also approximately equal. Suspiciously, they concluded they were observing the same object but with two images. And this was the first gravitational lensing [38–40] effect ever observed, which was a consequence of GR of Einstein: massive objects lying between a source (e. g., a quasar) and an observer should act as a lens to bend the spacetime and, consequently, light from this source. The more massive the object, the stronger will be the lensing effect. After this, many more lensing effects were observed, even for entire clusters of galaxies, as the ones observed in Figure 4, and therefore we could calculate more accurately the mass of such systems and these calculations suggested there was 10 times more matter than we could actually see.

Around this time there was a consensus among the cosmologists that DM might be composed by sub-atomic particles [41, 42] and this is where particle physics comes in. Besides this stream of observations of gravitational lensing, anisotropies were detected in the CMB possibly due to the gravitational potential of DM and its effects on the density and velocity of ordinary matter. These results were first observed in 1992 by COBE [43, 44] (or Explorer 66) and were later, in 2013 (Planck spacecraft), observed with more precision.

In view of the experimental observations, modified theories of gravity like Modified Newtonian Dynamics (MOND) [45] (Modified Newtonian Dynamics), are still being explored today. The DM hypothesis remains still a strong theoretical approach to describe this missing matter problem. Collaborations, such as the MAssive Compact Halo Objects (MACHOs) [46] and the EROS collaborations [47] also tried to find

very massive objects to try to account for this factor of 10, previously mentioned, in these interstellar systems, such as neutron stars, black holes and others. Although they detected some signals between 1993 and 2000, these objects weren't still numerous enough to account for all the mass needed and the collaborations put an upper limit in the range of 8% and 50% to what the amount of missing matter should be DM.

We reached the 2000s knowing DM is not made of gas and/or MACHOs (black holes, neutron stars...) either. And finally, in 2004 we got the first direct evidence of the existence of DM with the discovery of the galaxy cluster 1E 0657-56, also known as the "Bullet Cluster", by Douglas Clowe, Anthony Gonzalez and Maxim Markevich [48] (Figure 5). This cluster was formed after the collision of two large clusters of galaxies moving with great speeds and it is located about 3.8 billion light years from Earth.

Figure 5: Bullet cluster. We have an X-ray image (pink) superimposed over a visible light image (galaxies), with matter distribution calculated from gravitational lensing (blue).

Hot gas detected by the Chandra Observatory in X-rays is seen as two pink clumps in the image and contains most of the baryonic matter in the two clusters. The bullet-shaped clump on the right is the hot gas from one cluster, which passed through the hot gas from the other larger cluster during the collision. The blue areas in the image show where astronomers find most of the mass concentration in the clusters, which is determined through the effect of gravitational lensing. Most of the matter in the clusters (blue) is clearly separate from the normal matter (pink), giving direct evidence that nearly all of the matter in the clusters is dark. The hot gas in each cluster was slowed by a drag force during the collision. In contrast, the DM was not slowed by the impact because it does not interact directly with itself or the gas except through gravity. Therefore, during the collision, the DM clumps from the two clusters moved ahead of the hot gas, producing the separation of the dark and normal matter seen in the image. If hot gas was the

most massive component in the clusters, as proposed by alternative theories of gravity, such an effect would not be seen. Instead this result shows that DM is required.

1.4.2 Some hypothesis for what DM could be

In modern astrophysics, cosmology and particle physics there have been numerous hypothesis to describe the interactions between DM and the particles of the SM and try to find a viable candidate for a DM particle. We know that DM doesn't emit light, doesn't absorb it and that's why it's extremely difficult for us to see it, but we know it interacts with particles through gravity (e.g., gravitational lensing). Some of these hypothesis are listed below:

- **Modified gravity theories** - because DM has not yet been observed and the observations mentioned in the previous section point out that something is missing, these modifications to gravity theories have emerged to explain these observational phenomena without introducing a new unknown type of matter. In principle, a suitable modification to GR can eliminate the need for DM. Among these theories are MOND [45] and its relativistic generalization Tensor-Vector-Scalar Gravity (TeVeS) [49], f(R) gravity [50], entropic gravity [51], just to name a few. The problem with these alternative hypothesis is that observational evidence for DM comes from so many independent approaches (galaxy rotation curves, velocity dispersions, gravitational lensing, CMB anisotropies, and others that weren't mentioned). Explaining any individual observation is possible but explaining all of them in the absence of DM is very difficult. Nonetheless, there have been some scattered successes [52, 53] for these theories. However the prevailing opinion among most astrophysicists is that there is probably enough data to conclude there must be some form of DM present in the Universe.

- **New particles** - since we believe that DM may be composed by a (new) subatomic particle, we theorized about many different ones that might exist, due to the different kinds of states of DM we hypothesized.

  - **Axion** - is a scalar (spin-0) hypothetical elementary particle, neutrally charged postulated by the Peccei-Quinn theory in 1977 to resolve the strong CP problem in QCD and it interacts weakly with light and other types of matter. Axion's mass is predicted to be within a narrow specific range - 10^{-5} to 10^{-3} eV/c^2 [54] - and they are of interest as a possible component of Cold Dark Matter (CDM) being perhaps the strongest candidate as a DM particle.
  - **Weakly Interacting Massive Particles (WIMPS)** - are hypothetical particles with no formal definition, but broadly, a WIMP is a new elementary particle which interacts via gravity and any other force (or forces). Many WIMP candidates are expected to have been produced thermally in the early Universe [55] and constitute also CDM. Despite the absence of a more detailed physical description, an extension of the Supersymmetry (SUSY) model, called

Minimal Supersymmetric Standard Model (MSSM), predicts the existence of a particle called "neutralino" [56] (spin-$1/2$) which is today a candidate for a WIMP DM particle. Neutralinos don't have a very well defined mass, theories predicting them to be above 300 GeV and a lightest neutralino is the leading WIMP DM candidate. WIMP particles are also predicted by universal extra dimension and little Higgs theories and many other extensions of the SM;

  - **Other (more exotic) particles** - to solve the cuspy halo problem [57] - discrepancy between the inferred DM density profiles of low-mass galaxies and the density profiles predicted by cosmological N-body simulations - a state of CDM called "fuzzy cold dark matter" [58] was proposed that would consist of extremely light scalar particles with masses of $\approx 10^{-22}$ eV.

- **Primordial Black Holes (PBHs)** - they belong to the class of MACHOs discussed previously and are hypothetical black holes that formed soon after the Big Bang. PBHs are non-baryonic and, as such, are plausible DM candidates [59].

If DM is made up of subatomic particles, then possibly billions of such particles must pass through every square centimeter of the Earth each second. Many experiments aim to test this hypothesis and we can divide them into two classes: (1) the direct detection experiments that aim to observe low-energy recoils (few keV) of nuclei induced by interactions with particles of DM (which we assumed are passing through the Earth) and after such a recoil the nucleus will emit energy in the form of scintillation light or phonons, as they pass through sensitive detection apparatus; (2) and the indirect detection experiments which search for the products of the self-interaction or decay of the DM particles in outer space (e.g. two DM particles could annihilate to produce gamma rays or SM particle-antiparticle pairs).

An alternative approach to the detection of DM particles in nature is to produce them in a laboratory. Experiments with the LHC may be able to detect DM particles produced in proton-proton collisions. Since a DM particle should have negligible interactions with visible matter, it may be detected indirectly as large amounts of missing energy and momentum that escapes the detectors.

1.4.3 Simplified models and our approach

Simplified models [60–62] use an effective lagrangian describing the interactions of a small set of particles relevant for a specific process. Consequently, they have a smaller number of free parameters. Deviations from the phenomenology of these models can be taken as evidence for a larger set of particles playing a role in new physics, making way for building more accurate models. Moreover, parameters, such as masses and cross-sections, are directly related to collider physics observables, making the simplified model approach an effective framework for evaluating searches and a useful starting point for characterizing positive signals of new physics.

In this work we made use of a simplified model [15] that assumes DM is described by a single WIMP, X_D, which is a Dirac fermion and interacts with the SM through the exchange of a mediator (a new field), ϕ, in the scalar case, and A in the pseudo-scalar case. To simplify the notation, we will use Y_0^+ for the

scalar boson and Y_0^- for the pseudo-scalar boson. Also, this model assumes this mediator is not part of the SM. The interaction lagrangians between the mediator and the DM particle and the SM particles are given, respectively, by:

$$\mathcal{L}_{X_D}^{Y_0} = \overline{X}_D(g_{X_D}^S + ig_{X_D}^P\gamma_5)X_D Y_0 \tag{1.19}$$

$$\mathcal{L}_{SM}^{Y_0} = \sum_{i,j}\left[\bar{d}_i\frac{y_{ij}^d}{\sqrt{2}}(g_{d_{ij}}^S + ig_{d_{ij}}^P\gamma^5)d_j + \bar{u}_i\frac{y_{ij}^u}{\sqrt{2}}(g_{u_{ij}}^S + ig_{u_{ij}}^P\gamma^5)u_j\right]Y_0 \quad , \tag{1.20}$$

where $g_{x_D/u_{ij},d_{ij}}^{S/P}$ are the scalar/pseudo-scalar couplings of DM (X_D) and quarks (u_{ij}, d_{ij}). As we can see, this proposed model can be simplified to have very few free parameters, depending on the couplings to the SM and to the DM mediator and the masses m_{X_D} and m_{Y_0}. As we will see later, our main focus was on the search for this mediator (spin-0 boson) with mass equal to zero given the motivation mentioned previously. Therefore, in practice, we have considered Y_0 to be a DM particle.

2

Experimental Setup

In this chapter, an overview of the LHC is given as well as a description of one of its main experiments, ATLAS, the largest general-purpose particle detector at the LHC. It has been a challenge, since Run 1, the production of DM particles in the laboratory, which may profit from new upgrades that are constantly being made to the detector and the LHC. With Run 3 currently going on, we hope to see already some new experimental hints of DM, as we managed to increase the center of mass energy and the luminosity of the collider allowing us to generate more events and, possibly, detect these new particles. The work discussed in this thesis required the simulation of a generic detector, which, in our case, was performed by DELPHES, described at the end of this chapter.

2.1 Large Hadron Collider (LHC)

The LHC is the largest and highest-energy particle accelerator in the world and is located at CERN, in Geneva, Switzerland. The CERN accelerator complex is represented Figure 6. It was built between 1984 and 1989 and if first started on the 10th September 2008. It consists of a 27 km ring of superconducting magnets in an underground environment at about 100 m deep, with a number of accelerating structures to boost the energy of the particles along the way.

Inside the accelerator, two high-energy beams travel in opposite directions, which are guided by a strong magnetic field maintained by superconducting electromagnets, in separate beam pipes. These beam pipes are kept at an ultra-high vacuum to ensure the beam quality, and operate at a temperature of 1.9 K to enable the superconductivity properties in the magnets. We achieve these temperatures by connecting the accelerator to a distribution system of liquid helium.

As the beams approach the detectors along the ring, they are radially confined and crossed to induce particle collisions in well-defined interaction points. Particles in the LHC beams are packed in bunches along the beam direction. The LHC was designed to collide proton beams with a center-of-mass energy $\sqrt{s}$ of up to 14 TeV with a projected nominal instantaneous luminosity of 10^{34} cm^{-2} s^{-1}. It also collides heavy (Pb) ions with an energy of 2.8 TeV per nucleon with a peak luminosity of 10^{27} cm^{-2} s^{-1}. As of today, we are currently on Run 3, where we reached a center-of-mass energy for proton collisions of 13.6 TeV.

In Figure 7 is represented a schematic plan of the different upgrade stages of LHC, later becoming a HL-LHC.

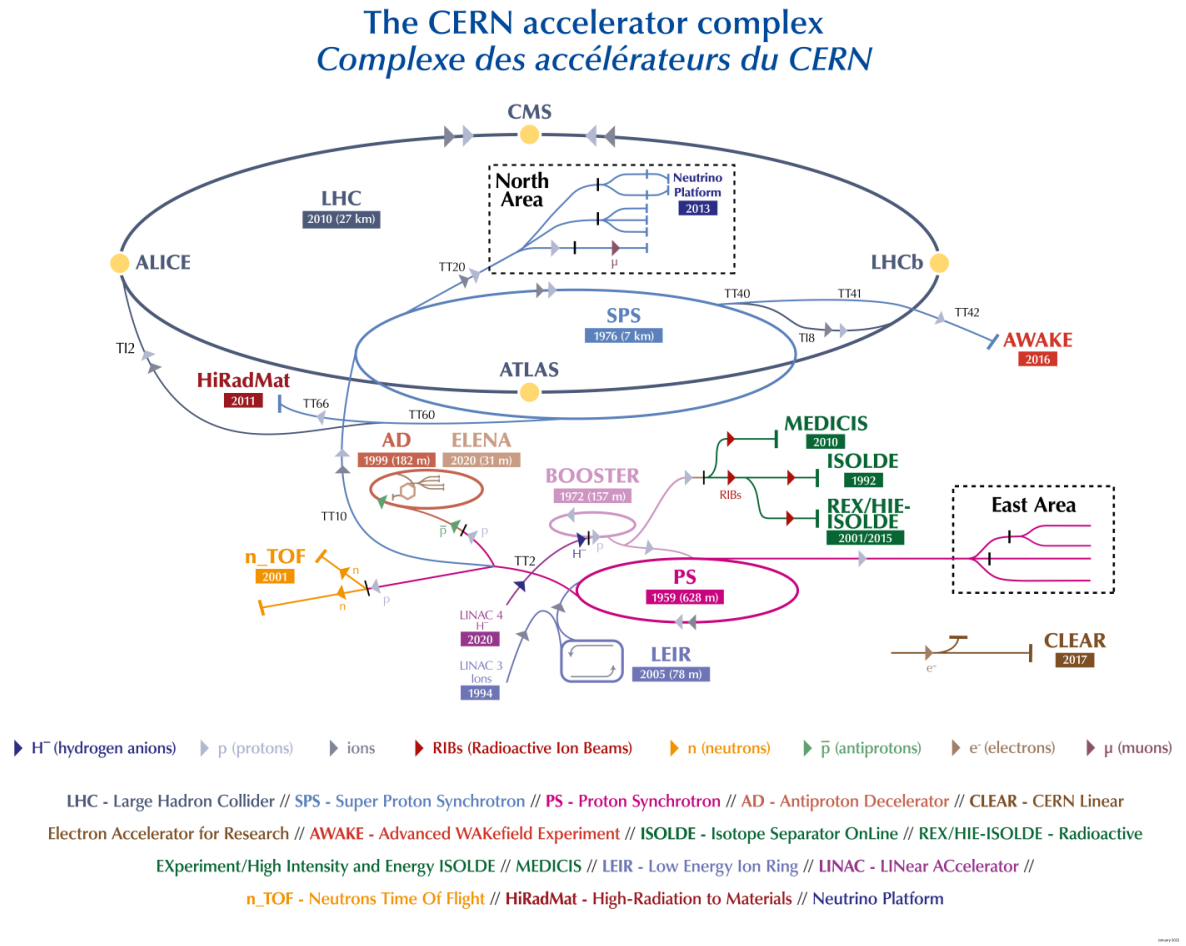

Figure 6: CERN accelerator complex.

The high luminosity delivered by the LHC also gives rise to a challenge for the experiments, since that, after the inelastic pp collisions per bunch crossing (expected 24), we have an overlay of secondary collisions events that is known by pile-up.

So far the LHC has been gone through two long shutdown periods, being currently in the early stages of its third run, expected to last until 2025 before its third long shutdown period. This will most likely be its final shutdown before it can operate with the highest center-of-mass energy the accelerator was designed (Run 4) - 7 TeV of energy per proton beam and colliding at a center-of-mass of 14 TeV - which is scheduled to start in 2029.

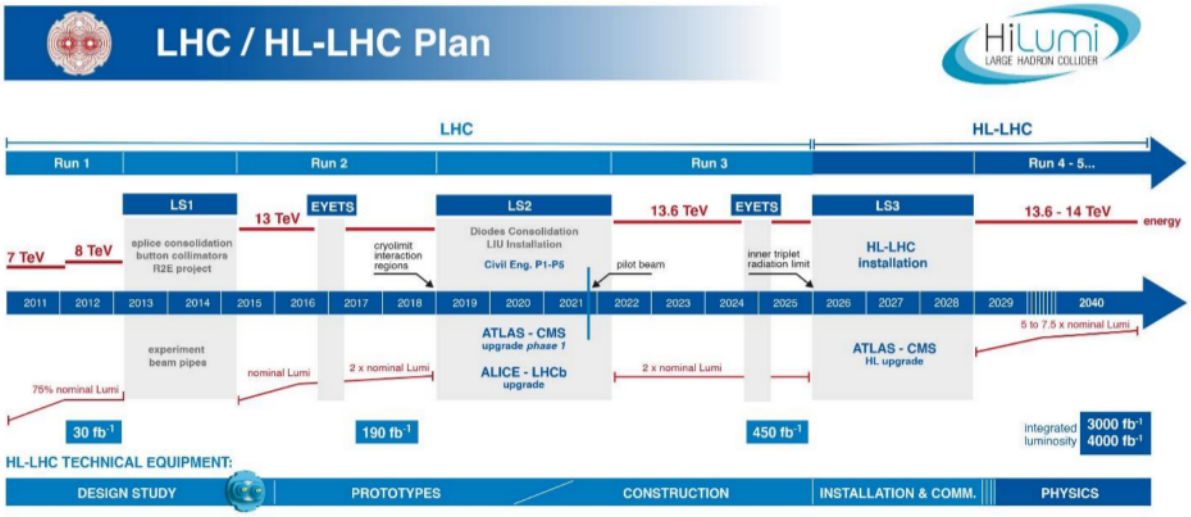

Figure 7: Timeline of the LHC and future plans to become a HL-LHC. The long shutdown periods (upgrades) are shown, as well as the schedules for the past Runs and for the Runs to come.

2.2 ATLAS detector

ATLAS was designed and built for probing pp and lead ion collisions (PbPb), being able to perform a wide range of precise measurements and having sensitivity to new physics processes. New phenomena are still expected to occur at the TeV scale, thus defining the requirements for the detector features.

The search for the SM Higgs boson has been used as a benchmark to establish the performance of important sub-systems of ATLAS. For example, the decay of the Higgs boson into a photon pair requires good electromagnetic calorimetry. On the other hand, the predomninant decay mode $H \longrightarrow b\bar{b}$, which is expected to have a large QCD background, requires good b-tagging effiency, only attained with fine vertex reconstruction. And in the case of final states with W bosons decaying leptonically, the presence of neutrinos adds the requirement of a good reconstruction of missing transverse energy. Other physics goals that served as a starting point to determine the design of the ATLAS detector were the search for new heavy gauge bosons W' and Z', supersymmetric particles and experimental signatures of the existence of extra dimensions. Moreover, since we have large amounts of pile-up at the LHC, we require mechanisms for resolving the different interaction vertices in a single bunch crossing, thus relying on high precision tracking.

ATLAS uses a right-handed reference system in which the origin of this coordinate system is defined by the nominal IP in the center of the detector while the beam direction defines the z-axis and the $x-y$ plane is transverse to the beam direction. The positive x-axis is defined as pointing from the IP to the centre of the LHC ring and the positive y-axis is defined as pointing upwards. Polar coordinates (r, ϕ) are used in the transverse plane, ϕ being the azimuthal angle around the beam pipe. The polar angle θ is the angle from the beam axis and the pseudorapidity is defined as $\eta = -ln(tan(\theta/2))$. The distance ΔR in the pseudorapidity-azimuthal angle space is defined as $\Delta R = \sqrt{\Delta\eta^2 + \Delta\phi^2}$.

The ATLAS detector is forward-backward symmetric with respect to the interaction point and it consists of multiple cylindrical layers. ATLAS is 25 m tall and 44 m long, with a mass of approximately 7000 tonnes. Its innermost sub-system is the Inner Detector (ID), that is immersed in a 2 T solenoidal magnetic field and it reconstructs the tracks of charged particles. Outside the ID, there is the electromagnetic (EM) calorimeter, which is a lead and LAr detector with accordion-shaped layers where photons and electrons are contained. Next, there are the hadronic calorimeters, which are composed of scintilating tiles in the central region ($|\eta| < 1.7$) and are LAr-based in the forward region ($|\eta| > 1.5$), where hadrons are contained and deposit their energy. Finally, the muon-tracking chambers, which make up the outermost layers of ATLAS, are immersed in a magnetic field created by toroid magnets. The overall ATLAS detector layout is shown in Figure 8.

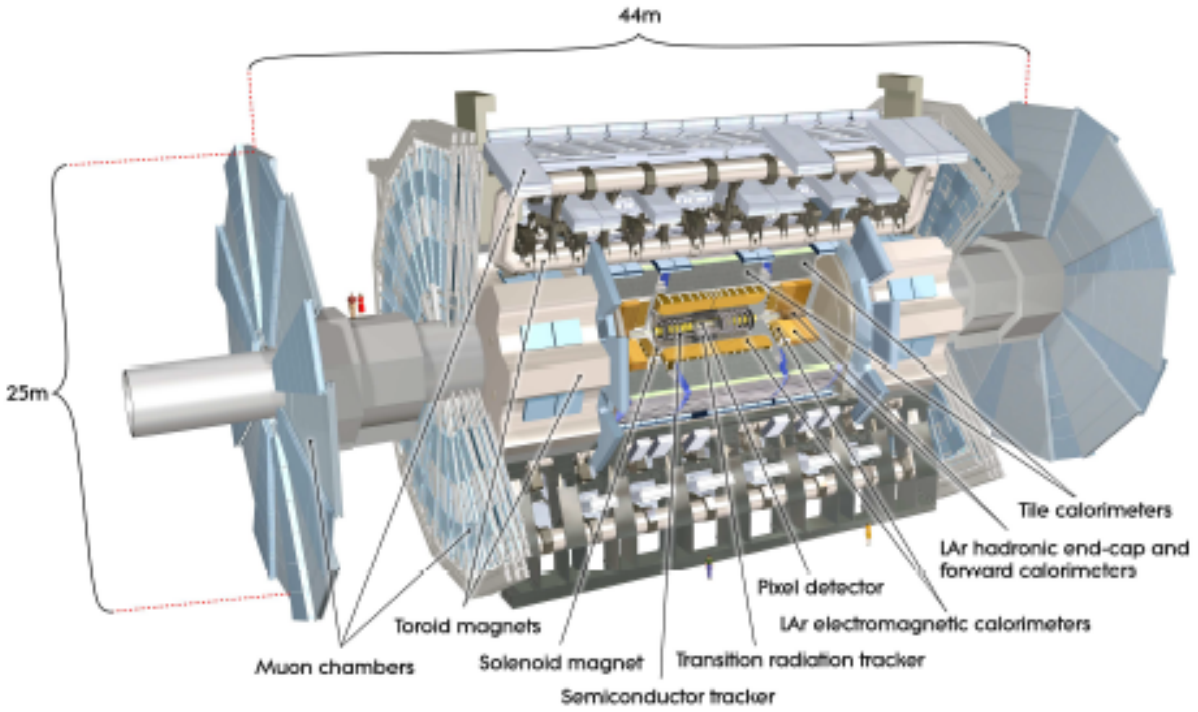

Figure 8: Cutaway view of the ATLAS detector. The subdetectors and main systems are identified, and two people are visible on the image for scale.

2.2.1 Inner detector (ID)

The ID is a tracking system designed to provide excellent momentum resolution and precise reconstruction of interaction vertices for charged particles. The momentum measurement relies on the curvature of the particle trajectories, which are bent by a magnetic field peaking at 2 T and pointing along the z-axis, which is provided by a solenoid magnet placed immediately outside the ID. Since approximately 1000 particles will emerge from the IP every 25 ns, creating a very large track density in the detector, the ID is also equipped with three independent but complementary sub-detectors to achieve such high momentum and vertex resolution required by the benchmark physics processes: the pixel detector, the Semiconductor Tracker (SCT) and the Transition Radiation Tracker (TRT), each with structures covering the barrel region and the end-cap regions.

The pixel detector along the barrel region is arranged on concentric cylinders around the beam axis, while in the end-cap regions they are located on disks perpendicular to the beam axis and it has approximately 80.4 million readout channels. The SCT is composed of silicon strips disposed in four concentric cylinders in the barrel region around the beam axis, and the two end-caps contain nine disk layers and the number of readout channels is approximately 6.3 million. The TRT consists of 4 mm diameter straw tube detectors with a gold-plated wire running inside. In the barrel region, the straws are parallel to the beam axis and are 144 cm long, and in the end-cap region, 37 cm long straws are arranged radially in wheels. The total number of TRT readout channels is approximately 351000. The electron identification capabilities are enhanced by the detection of transition-radiation photons in the xenon-based gas mixture of the straw tubes. Figure 9, below, shows a cutaway view of the ID.

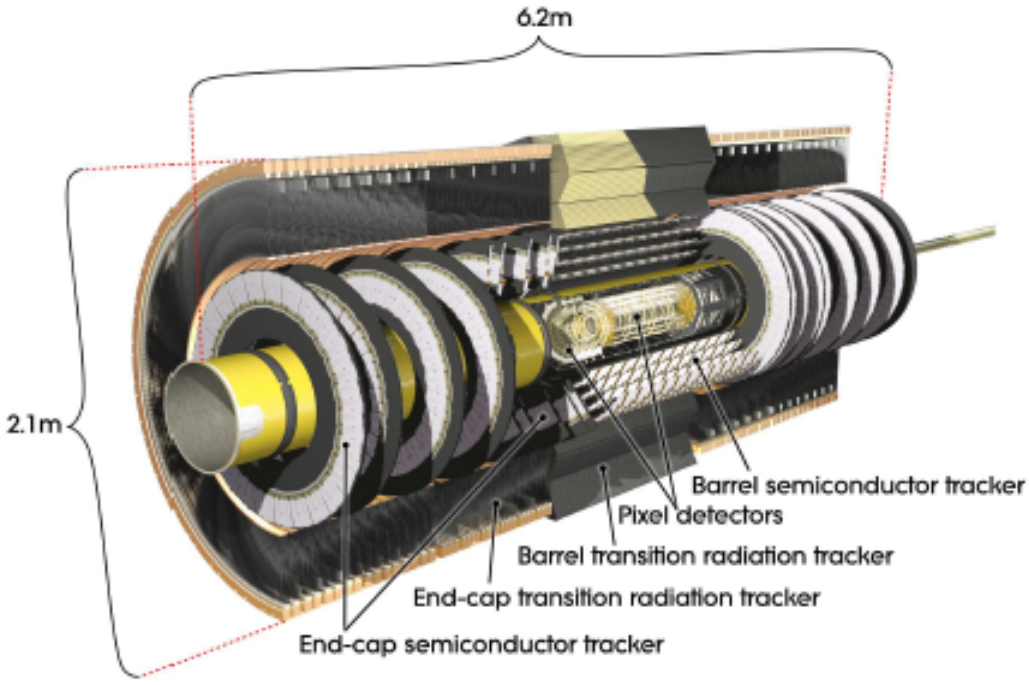

Figure 9: Cutaway view of the inner detector with all of its components labeled.

2.2.2 Electromagnetic (EM) calorimeter

The EM calorimeter is the detector layer where most photons and electrons are contained, and in which EM-interacting particles leave energy deposits. This calorimeter is divided into a barrel part ($|\eta| < 1.475$) and two end-cap components ($1.375 < |\eta| < 3.2$). The central solenoid and the LAr calorimeter share a common vacuum vessel, in the barrel region, which consists of two identical half-barrels separated by a small gap of 4 mm at $z = 0$, and this vessel is what keeps the low temperature for the LAr. In the end-caps, the EM calorimeter is made up from two coaxial wheels: an outer wheel covering the region $1.375 < |\eta| < 2.5$, and an inner wheel covering the region $2.5 < |\eta| < 3.2$. This calorimeter is composed of accordion-shaped layers of lead absorber plates, LAr and kapton electrodes, as one can see in Figure 10. The accordion geometry provides complete ϕ symmetry without azimuthal cracks. The high-density lead plates act as absorber elements and are used as inducement for particle showers, ensuring the energy dissipation of particles like electrons and photons. Since they give a large effective depth to the calorimeter, they prevent these particles from piercing through into the outer layers of the detector. As particles in the shower cross the LAr layers - the active element - the argon gets ionized, creating, this way, a current in the electrodes which is detected and recorded. Only a fraction of the energy of these particles in the showers is deposited in this way. From this sample of deposited energy, one can estimate the total energy and its spatial distribution.

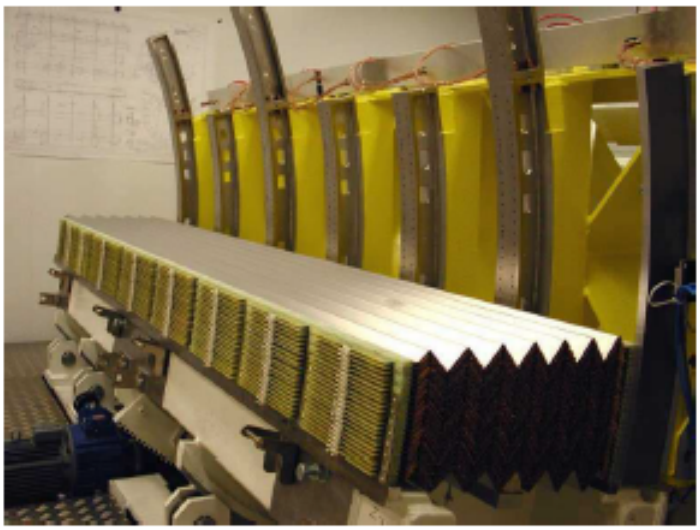

Figure 10: Photograph of a partially stacked barrel electromagnetic LAr module, where is visible the accordion geometry.

2.2.3 Hadronic Calorimeter

The hadronic calorimeter is a sub-detector where hadrons that were not contained by the EM calorimeter are ultimately contained and deposit their energy, which is then measured through sampling. This calorimeter is composed by the Tile Calorimeter (TileCal), which is placed directly outside the EM calorimeter envelope that covers the barrel region, and by two end-cap calorimeters: the LAr hadronic end-cap calorimeter, that consists of two independent wheels per end-cap; and the LAr forward calorimeter, a high density cylinder which provides both EM and hadronic calorimetry in a region of larger $|\eta|$. Individually, the TileCal is divided in a central barrel, which covers the region $|\eta| < 1.0$, and two extended barrels covering the range $0.8 < |\eta| < 1.7$. These three barrels are divided azimuthally into 64 modules, and range radially from an inner radius of 2.28 m to an outer radius of 4.25 m. It's a sampling calorimeter using steel as the absorber and plastic scintillating tiles as the active material. These tiles emit light as they are crossed by ionising particles. This emitted light is then collected by optical wavelength-shifting fibers at the edges of each tile into two seperate photomultiplier tubes (PMT) that generate the readout signal. The previously mentioned wheels per end-cap present in the LAr hadronic end-cap calorimeter are located directly behind the end-cap EM calorimeter and they cover the region with $1.5 < |\eta| < 3.2$. Each wheel is built from 32 azimuthal modules and are composed of 25 mm copper plates, which are closest to the IP, 50 mm for plates further away. The copper plates are interleaved with 8.5 mm LAr gaps, providing the active medium for this sampling calorimeter. The LAr Forward Calorimeter (FCal) is a cylindrical structure integrated in each of the end-cap wheels of the LAr hadronic calorimeter. It consists of three modules in each end-cap: the first, made of copper, is optimised for EM measurements, while the other two, made of tungsten, measure the energy of hadronic interactions. Each of these modules consists of a metal matrix, with regularly spaced longitudinal channels filled with the electrode structure consisting of concentric rods and tubes parallel to the beam axis. The LAr in the gap between the rod and the tube is the sensitive medium.

2.2.4 Muon spectrometer

The ATLAS muon system serves the purpose of tracking and measuring the momentum of muons. Since these interact weakly with matter, they are not contained by the calorimeters. It is based on a complex arrangement of superconducting air-core toroid magnets which deflect the muon trajectories, high-precision tracking chambers and a dedicated muon trigger system. Figure 11 shows the layout of the muon spectrometer. Over the range $|\eta| < 1.4$, magnetic bending is provided by the large barrel toroid. For $1.6 < |\eta| < 2.7$, muon tracks are bent by two smaller end-cap magnets inserted into both ends of the barrel toroid. Over $1.4 < |\eta| < 1.6$, usually referred to as the transition region, magnetic deflection is provided by a combination of barrel and end-cap fields. Each of the toroids consists of eight superconducting coils assembled radially and symmetrically around the beam axis, which operate at a temperature of 4.6 K.

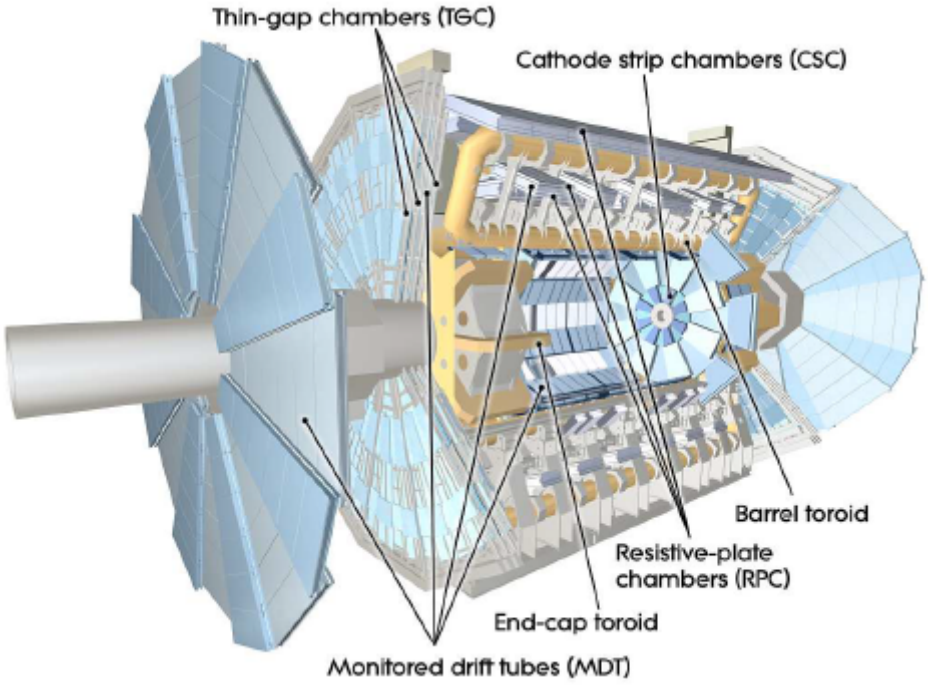

Figure 11: Cutaway view of the ATLAS muon system with its main components labeled.

The end-cap toroid coil system is rotated 22.5° with respect to the barrel toroid coil system in order to provide radial overlap and to optimise the bending power at the interface between the two coil systems (the transition region). The field produced in the central region is approximately 0.5 T on average and 3.9 T at its peak. In the end-caps, the field is approximately 1 T on average and 4.1 T at its peak.

The precision momentum measurement is performed by Monitored Drift Tube (MDT) chambers, covering the range $|\eta| < 2.7$. These chambers are composed of layers of drift tubes with an operation similar to the TRT in the ID, achieving an average resolution of about 35 μm per chamber. The ones in the barrel region are placed in three coaxial cylindrical layers around the beam axis. In the two end-cap regions, muon chambers form large wheels, perpendicular to the z-axis and located at distances up to 21.5 m from the IP. In the forward region ($2.0 < |\eta| < 2.7$), instead of MDTs, Cathode Strip Chambers (CSC) are used in the innermost layer, since they can handle higher hit rates and have finer time resolution. These are multiwire proportional chambers in which the cathode planes are segmented into strips running in perpendicular directions.

The precision tracking chambers are complemented by a system of fast trigger chambers. In the barrel region ($|\eta| < 1.05$) this is achieved with Resistive Plate Chambers (RPC), while in the end-cap ($1.05 < |\eta| < 2.4$) Thin Gap Chambers (TGC) are used. The objective for the design was to minimise time contributions from signal propagation and electronics to allow efficient identification of the beam crossing. Both chamber types deliver signals with a spread of 15-25 ns, allowing each individual chamber to tag the bunch crossing with efficiency of at least 99%.

2.2.5 Forward detectors

In addition to the main ATLAS detector systems described previously, three smaller sets of detectors were built to provide good coverage in the very forward region. The first system is a Cherenkov detector called LUCID [63] (LUminosity measurement using Cherenkov Integrating Detector). It's the only detector which is primarily dedicated to relative luminosity monitoring in ATLAS and it is located at a distance of ± 17 m from the IP. Its main purpose is to detect inelastic pp scattering in the forward direction, in order to both measure the integrated luminosity and to provide online monitoring of the instantaneous luminosity and beam conditions. The second system is the Zero-Degree Calorimeter (ZDC), located at a distance of ± 140 m from the IP. Its primary purpose is to detect forward neutrons with $|\eta| > 8.3$ in heavy-ion collisions. It plays a key role in determining the centrality of such collisions, which is strongly correlated to the number of very forward neutrons and it will provide additional minimum-bias trigger for ATLAS. And the third detector is the most remote detector called ALFA (Absolute Luminosity For ATLAS) located at a distance of approximately ± 240 m from the IP. It consists of scintillating-fibre trackers located inside Roman pots and, like the name says, its objective is to measure the absolute luminosity of the collider via elastic scattering at small angles ($\sim 3\mu rad$), through the usage of the optical theorem. We can see how the detectors are placed according to their distance from the IP in Figure 12.

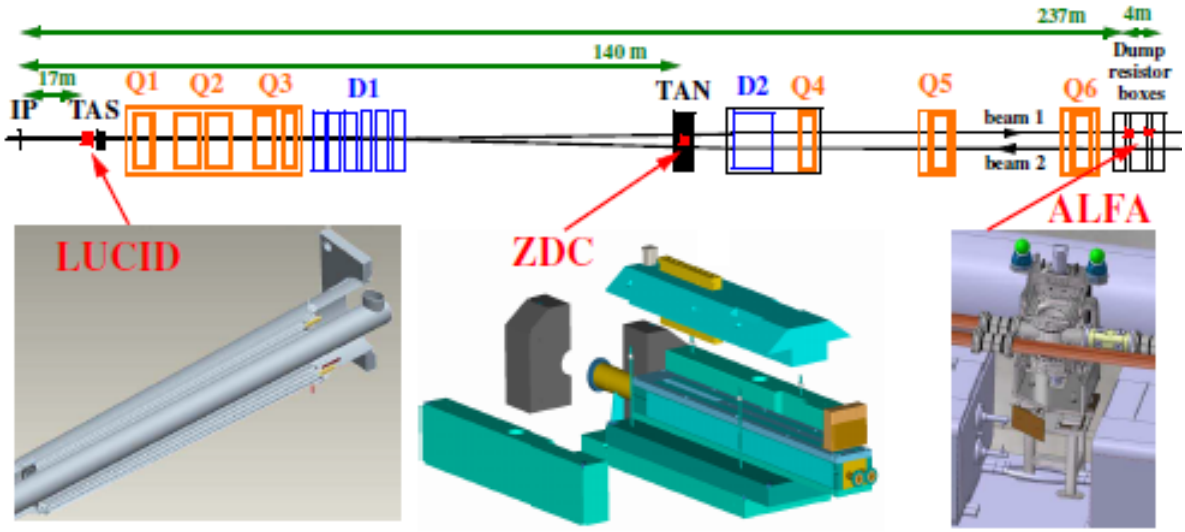

Figure 12: Placement of the forward detectors along the beam-line around the ATLAS IP.

2.2.6 Trigger system

The ATLAS trigger system has three distinct levels: the Level-1 (L1), Level-2 (L2) and the event filter. Each trigger level refines the decisions made at the previous level and, where necessary, applies additional selection criteria.

The L1 trigger is the first rate-reducing step, based on custom-made electronics and it searches for high p_T muons, electrons, photons, jets and τ-leptons decaying into hadrons as well as large missing E_T.

The L1 level is configured such that it makes a decision in less than 2.5 μs to select an event and to define one or more Region of Interest (RoI) in the detector, i.e. the information about the coordinates η and ϕ of the interesting feature, the type of this feature (electromagnetic, hadronic, muon...) and the criteria passed, e.g. a threshold. This first level trigger deliver an output event rate to approximately 75 kHz.

The L2 selection is seeded by the L2 information provided by the L1 trigger over a dedicated data path. L2 selections use all the available detector data within the L2s - approximately 2% of the total event data. The L2 systems are designed to reduce the trigger rate to around 3.5 kHz, with an event processing time of about 40 ms, averaged over all events.

The final stage of the event selection is carried out by the event filter, which reduces the event rate to roughly 200 Hz. Its selections are implemented using offline analysis procedures, allowing the permanent storage of the data, within an average event processing time of the order of 4 s. These two higher levels lead up an event size of approximately 1.3 Mbytes.

2.2.7 Object reconstruction

2.2.7.1 Electrons and photons

For the reconstruction of electrons and photons, clusters out of the energy deposits in the EM calorimeter are built. Then all the reconstructed tracks in the ID are scanned, looking for one that loosely matches one of the clusters. Additionally, the candidate is flagged if it matches a photon conversion reconstructed in the ID. Electron and photon candidates are thus separated reasonably cleanly, by requiring the electrons to have an associated track but no associated conversion, in contrast to the photons, that are defined as having no matched track, or as having been matched to a reconstructed conversion. In order to identify electrons a set of reconstruction properties are used, such as the ratio of energy (measured by the calorimeter) to momentum (measured by the ID), the difference between the coordinates η and ϕ reconstructed by the cluster and the track extrapolated into the calorimeter, and the transition radiation hits on the track.

The energy of high-p_T electrons is obtained from the energy measured in the calorimeter. On the other hand, the η and the ϕ directions are more precisely determined using the associated track. The standard identification for isolated high-p_T electrons is based on cuts on the shower shapes, on information from the reconstructed track and on the combined reconstruction. Three sets of cuts have been studied depending on the signal efficiency and jet rejection requirements of the physics samples under study: we have the "loose cuts" which consists of simple shower-shape cuts and very loose matching cuts between reconstructed track and calorimeter cluster; "medium cuts", which add shower-shape cuts using the important information contained in the first layer of the EM calorimeter; "tight cuts" that tighten the track-matching criteria and the cut on the energy-momentum ratio.

For photon, everything is derived from the calorimeter information, the energy, the ϕ-direction and the η-direction. However, photons are much harder to extract as a signal from the jet background than certain specific isolated electron signals, such as those expected from the decay of a vector boson. A single set of

photon identification cuts, equivalent to the "tight cuts" defined for electrons, has been optimised relying on the shower shapes in the calorimeter with a focus on separating single π^0 mesons from photons using the very fine granularity in η of the silicon strip layer. Multivariate methods have also been developed for the more difficult case of photon identification, but they will not be approached here.

In addition to the calorimeter-seeded electron and photon reconstruction, a second electron reconstruction and identification algorithm uses good-quality tracks as a seed and constructs a cluster around the extrapolated impact point in the calorimeter. This algorithm relies more on the electron identification capabilities of the inner detector and has been developed to improve the efficiency for low-p_T electrons as well as for electrons close to jets.

2.2.7.2 Muons

The collisions at the LHC will produce a broad spectrum of final-state muons, ranging from low-momentum non-isolated muons in b-jets to high-momentum isolated muons from W/Z-boson decays. Muon measurements are a combination of accurate measurements in the muon spectrometer and in the ID. The muon spectrometer also efficiently triggers on muons over a wide range of energies and over $|\eta| < 2.4$ and toroidal field guarantees excellent momentum resolution even at the highest values of η. Momentum measurements are performed using combined tracks from the ID and the muon spectrometer. The ID resolution provides the best measurement at low to intermediate momenta, whereas the muon spectrometer takes over above 30 GeV. When performing these momenta measurements, muon tracks from the spectrometer are propagated back to the IP and this requires a momentum correction for the energy that was lost in the calorimeters. This lost energy is estimated by an algorithm which uses either the parametrised expected energy loss or the measured calorimeter energy, but only if it exceeds significantly the most probable energy loss and if the muon track is isolated.

2.2.7.3 Jets

Since there is a wide variety of physics processes of interest at the LHC that produce jets, a variety of jet clustering algorithms using as input any reconstruction object having four-momentum representation, such as final-state particles for truth-particle jets (only available in simulated data) and calorimeter signals, were implemented. The two default jet-clustering algorithms, followed by a calibration step, in ATLAS are a seeded fixed-cone algorithm and a successive recombination algorithm, or $k_\perp$ algorithm.

The seeded cone algorithm uses two parameters, the transverse energy threshold for a seed, E_T =1 GeV for all cone jets, and the cone size, $\Delta R = \sqrt{(\Delta\eta)^2 + (\Delta\phi)^2}$, with $\Delta R = 0.4$ for narrow jets and $\Delta R = 0.7$ for wide jets. The cone algorithm in this particular implementation is fast and therefore also used in the high-level trigger.

The $k_\perp$ algorithm, however, was built to be more efficient for a large number of input objects and avoids the unusual pre-clustering step, making this algorithm the most used in ATLAS. The distance parameter $R = \sqrt{(\Delta\eta)^2 + (\Delta\phi)^2}$ is adjusted for narrow jets to $R = 0.4$ and for wide jets to $R = 0.6$.

These algorithms are applied over topological cell clusters that represent an attempt to reconstruct three-dimensional energy depositions in the calorimeter. First, the nearest neighbours are collected around seed cells with a significant absolute signal above the major seed threshold, $|E_{cell}| > 4\sigma_{cell}$ of the total noise (electronics plus pile-up). These neighbouring cells are collected independently of the magnitude of their own signal. If the absolute value of their signal significance is above a secondary seed threshold, typically such that $|E_{cell}| > 2\sigma_{cell}$, they are considered secondary seeds and their direct neighbours are also collected. Finally all surrounding cells above a very low threshold (typically set to 0σ) are added if no more secondary seeds are among the direct neighbours. A final analysis of the resulting cluster looks for multiple local signal maxima. In the case of more than one maximum in a given cluster, it is split into smaller clusters along the signal valleys between the maxima.

2.2.7.4 Missing transverse energy

Neutral particles that interact weakly with particles of the SM, such as neutrinos, evade detection in conventional collider detectors, therefore, not causing any observable response in the detector components. Detecting the presence of these particles requires deducing their existence based on the discrepancy in total momentum. This mismatch in vector momentum, specifically in the plane perpendicular to the direction of the particle beam, is referred to as missing transverse momentum, denoted as $\boldsymbol{p}_T$. The magnitude of this imbalance is known as Missing Transverse Energy (MET), often represented by $\not{E}_T$ or E_T^{miss}. Accurately measuring the MET is crucial for investigating various physics channels within the ATLAS experiment, particularly in the pursuit of identifying signals BSM, such as DM, SUSY, or extra dimensions.

The E_T^{miss} reconstruction in ATLAS is based in a first step on the calibrated calorimeter cell energies and on the reconstructed muons. The E_T^{miss} muon term is calculated from the momenta of the muons measured using the stand-alone muon-spectrometer reconstruction. This way, the energy lost by the muons in the calorimeter is not counted twice, since it is only taken into account in the calorimeter term. Only good-quality muons with a matched track in the ID are considered, which reduces considerably possible contributions from 'fake' muons, sometimes created from multiple hits in the muon spectrometer by highly energetic jets.

In a second step, the E_T^{miss} reconstruction accounts for a cryostat term, which corrects for the energy lost in the cryostat located between the barrel LAr EM and tile hadronic calorimeters.

Finally, a refined calibration of E_T^{miss} is performed through the association of each high-$\boldsymbol{p}_T$ reconstructed object, after being carefully ordered, in the event to its globally calibrated cell. The calibration of E_T^{miss} consists in replacing the initial contribution from globally calibrated cells by the contribution from the corresponding calibrated high-$\boldsymbol{p}_T$ objects. The cells which survive a noise cut and which are not associated to any reconstructed object are also calibrated using the global calibration scheme and accounted for the E_T^{miss} calculation.

2.2.7.5 b-tagging

The identification of b-quark jets, typically referred to as b-tagging, plays a vital role for the ATLAS experiment for both precise SM measurements, including the Higgs sector and for exploring new physics scenarios, which have a significantly extended reach thanks to the higher center of mass energy of the pp collisions delivered by the LHC. Only the jets with $p_T > 15$ GeV and $|\eta| < 2.5$ are considered for b-tagging and only reconstructed tracks within a distance $\Delta R < 0.4$ from the jet axis are used for b-tagging.

The basic b-tagging algorithms use charged particle tracks to produce a set of variables which discriminate between different jet flavour. Tracks are first associated to a jet and are then required to pass a quality selection based on their angular separation ΔR (track, jet) and this selection depends on each specific b-tagging algorithm. The ΔR association requirement varies as a function of the jet p_T, resulting in narrower cone for jets at high p_T which are more assembled. ATLAS uses three distinct b-tagging algorithms, which come up with complementary information:

- impact parameter based algorithm, which makes use of the signed impact parameter significance of the tracks matched to the jet. The sign is defined as positive (negative) if the point of closest approach of the track to the primary vertex is in front (behind) the primary vertex with respect to the jet direction;
- inclusive secondary vertex reconstruction algorithm (or secondary vertex finding algorithm, SV), that has the objective of reconstructing an inclusive displaced secondary vertex within the jet. It starts by reconstructing two-track vertices using the candidate tracks. Tracks are rejected if they form a secondary vertex which can be identified as likely originating from the decay of a long-lived particle, photon conversions or hadronic interactions with the detector material. A single vertex is then reconstructed using the tracks that survive this preselection;
- decay chain multi-vertex reconstruction algorithm, JetFitter [64], which exploits the topological structure of weak $b-$ and $c-$hadron decays inside the jet and tries to reconstruct the full primary vertex $\longrightarrow b \longrightarrow c-$hadron decay chain.

The output of these b-tagging algorithms are then combined in a multivariate discriminant which provides the best separation between the different jet flavours.

2.3 DELPHES

Usually, physics analyzes require a high level of accuracy and, therefore, experimental collaborations often rely on tools that fully simulate a detector's response. Such tools reproduce the interactions of long-lived particles with the detector matter content, the electronic response of each of the detector component and also the final observables which are reconstructed by means of complex algorithms. These procedures require computational resources that are only available to large collaborations.

However, in phenomenological studies like the one presented here, such a detailed simulation is not necessary and a parameterization of the detector response based approach is, generally, good enough. For this, we used the package DELPHES [18] to simulate the response of a general purpose detector, composed of an inner tracker, electromagnetic and hadronic calorimeters and a muon system. All are organized concentrically with a cylindrical symmetry around the beam axis. Moreover, properties, such as the detector active volume, the calorimeter segmentation and the strength of the magnetic field, can be chosen by the user.

2.3.1 Particle propagation

The first step carried by the simulation is the propagation of long-lived particles, for example electrons, protons, muons, through a uniform magnetic field (parallel to the beam direction) located in the inner detector volume. Neutral particles have a straight line trajectory, while charged particles follow a helicoidal trajectory until they reach the calorimeters. Particles that originate from a point outside the tracker volume are neglected.

The probability to reconstruct charged particles as tracks is set by the user as well as the energy and momentum resolutions depending on the particle type, p_T and η.

2.3.2 Calorimeters

After their propagation in the magnetic field, the particles reach the calorimeters: the Electromagnetic Calorimeter (ECAL), which is responsible for measuring the energy of the electrons and photons; and the Hadronic Calorimeter (HCAL) which measures the energy of charged and neutral (long-lived) hadrons. These calorimeters have a defined segmentation in a rectangular grid in (η, ϕ), although, for simplicity the segmentation is uniform in ϕ.

When these particles reach the calorimeters, they deposit a fraction of its energy in the corresponding ECAL (f_{ECAL}) and ECAL (f_{HCAL}) cells. By default, electrons and photons leave all their energy, having f_{ECAL} = 1, and the same thing happens to hadrons, f_{HCAL} = 1, except for kaons and Λ particles, which have f_{ECAL} = 0.3 and f_{HCAL} = 0.7. Muons, neutrinos and neutralinos do not deposit any energy in the calorimeters. The user can, however change this default setup and define more accurate values for these variables if one needs to.

Since ECAL and ECAL have equal segmentation, a straight line coming from the interaction point crosses one ECAL cell and one ECAL cell covering the same region in (η, ϕ). These pairs of cells are called calorimeter towers and are used in the object reconstruction, together with tracks.

The energy of each particle is concentrated in one single tower and the sum runs over all particles that reach the given tower. In order to avoid having to deal with discrete tower positions, an additional uniform smearing of the position over the cell range is applied.

2.3.3 Particle-flow reconstruction

The approach of particle-flow has the objective of obtaining the maximum amount of information provided by the various sub-detectors for reconstructing the event and it's based on the tracking system and the calorimeters. If the momentum resolution of the tracking system is better than the energy resolution of the calorimeters, then the tracking information within the tracker acceptance is more reliable to estimate the charged particles momenta. In real experiments, the tracker resolution is better than the calorimeter resolution only up to some energy threshold. Above this threshold, the calorimeter energy deposit is more reliable to estimate the momentum. However, in this phase of the simulation, the information provided from the tracker is always the most convenient one, if a track exists for a certain particle.

The particle-flow algorithm creates two sets of 4-vectors: the particle-flow tracks and the particle-flow towers, and these will serve as an input for the reconstruction of jets and $\not{E}_T$. Then, for each calorimeter tower, the energy deposited in the calorimeters originating from charged particles for which the track has been reconstructed is subtracted from the total energy deposited. If the remaining energy, E_{Tower}^{flow}, is positive a particle-flow tower is created with this remaining energy.

Being defined this way, it is implied that particle-flow tracks contain charged particles estimated with a good resolution, while particle-flow towers contain, in general, a combination of neutral particles, charged particles with no corresponding reconstructed track and additional excess deposits induced by the smearing of the calorimeters, and are characterized by a lower resolution. Despite the simplicity compared to what is required in real life experiments, this algorithm reproduces well the performance achieved at LHC.

2.3.4 Object reconstruction

- **Muons** - they have a probability of being reconstructed, but is zero beyond the acceptable range of the tracker and for momenta below a specified threshold to discard particles that exhibit looping behavior. The user determines this threshold. The muon's final momentum is achieved by applying a Gaussian smearing technique to the initial 4-momentum vector. The resolution of this smearing is determined by the user through a parameterization that depends on p_T and η.

- **Electrons** - reconstruction typically involves combining information from both the tracking system and the ECAL. However, DELPHES simplifies this process by expressing the reconstruction efficiency as a parameterized function of energy and η. Similar to muons, electron reconstruction efficiency becomes zero outside the acceptable range of the tracker and below a certain energy threshold. When it comes to energy resolution, a combination of the resolutions from the ECAL and the tracking system is utilized. Specifically, the tracking system resolution has more influence at low energies, while the ECAL energy resolution becomes dominant at higher energies.

- **Photons** - are reconstructed using only information from the ECAL. The reconstruction process disregards photon conversions into electron-positron pairs. The final energy of the photon is determined by applying the ECAL resolution to the original photon. Additionally, electrons that do not

have a reconstructed track but reach the ECAL are reconstructed as photons.

It is important to mention DELPHES does not include a fake rate for electrons, muons and photons. This fake rate parameterises the probability of a certain object (e.g., a jet) being misidentified as a lepton or a photon, and these are important, because, for example, in physical analyses with multi-lepton final states, we need to determine correctly the expected contribution of each background process to the analysis in question.

For a lepton or a photon to be reconstructed, an isolation criterion needs to be met. An object is said isolated if the activity in its vicinity is small enough. Such objects have small probability to originate from a jet. The isolation variable I for each reconstructed electron, muon or photon ($P = e, \mu, \gamma$) is defined as:

$$I(P) = \frac{\sum_{i \neq P} p_T(i)}{p_T(P)} \quad , \tag{2.1}$$

where the numerator is the sum of transverse momenta above a threshold p_T^{min} of all particles that lie within a cone of $\Delta R < R$ around that particle. P is said to be isolated if it verifies $I(P) < I_{min}$. The default values for these parameters are p_T^{min} = 0.1 GeV, R = 0.5 and I_{min} = 0.1 and they can be changed by the user.

2.3.5 Jets

In DELPHES, it is possible to generate jets using three different collections of objects, in which the user has the freedom to choose the jet clustering algorithm with the integrated package FASTJET [65], including the minimum threshold p_T for the jet to be stored in the final collection:

- generated jets - are gathered from generator level long-lived particles obtained after parton shower and hadronization;
- calorimeter jets - use calorimeter towers as input;
- particle-flow tracks and particle-flow towers

DELPHES also includes a module that automatically removes jets that have already been reconstructed as leptons or photons to avoid double-counting of particles in the final state.

2.3.5.1 b and τ jets

The algorithm for b and τ jet identification is as follows: the jet becomes a potential b jet or a τ candidate if its direction is within a certain ΔR cone of that jet axis. Given this, the probability for the jet to be identified as b or τ will depend on the parameterization the user defined for the tagging efficiency. The user can also specify a mis-tagging efficiency paremeterization, which is the probability that a particle other than a b or a τ has to be wrongly identified as such.

2.3.6 Missing E_T

Partons in the initial state having a negligible transverse momentum and the total transverse energy of undetected particles contribute to the E_T^{miss} and these can be assessed from the transverse component of the total energy deposited in the detector. This quantity can be estimated from one of the three sets of objects: generated particles, calorimeter towers, or particle-flow tracks and particle-flow towers.

3

Generation and event selection

The phenomenological analysis presented in this thesis, uses the dileptonic topology of the $t\bar{t}Y_0$ system which we want to study with angular observables. Our objective here is to adapt the current reconstruction algorithms we have used for the $t\bar{t}H$ production at the LHC and apply them to the $t\bar{t}Y_0$ system. We want to see how the mediator Y_0 affects our observables and the reconstruction of the $t\bar{t}$ system, once the angular distributions may depend on the scalar ($g^S_{u_{33}}$) and pseudoscalar ($g^P_{u_{33}}$) coupling constants of the top quarks to the DM mediator. In this chapter, the main steps of the phenomenological analysis, are described. We start with a description of the event generation and simulation followed by the selection of events. The details of the kinematic reconstruction of the $t\bar{t}$ system, the truth-matching procedure used to match the reconstructed tracks to the corresponding particles and, finally, the kinematic fit used to reconstruct the neutrinos and the intermediate heavy particles, are given.

3.1 Generation of signal and background

The signal event samples of $t\bar{t}Y_0$ were generated for proton-proton collisions at the LHC with a center-of-mass energy of 13 TeV using MadGraph5_aMC@NLO [66] at LO. The UFO model used was DMsimp_s _spin0 [15]. The mass of the top quark was set to m_t = 172.5 GeV and the W boson mass to m_W = 80.4 GeV. We set the mediator mass to m_{Y_0} = 0 GeV and the mass of the DM candidate was also fixed to zero (m_{X_D} = 0 GeV). We only considered non-vanishing couplings of the top quarks to the mediator ($g^{S/P}_{u_{33}} \neq 0$). All the other mediator couplings to quarks were set to zero. No decays were allowed for the mediator (Γ_{Y_0} = 0 GeV). The decay chains of heavy particles, such as top quarks and vector bosons, were performed by MadSpin [67], which ensures spin correlation effects to be preserved during particle decays. To simulate the parton shower and hadronization, Pythia was used [68]. For our signal we considered decays through the dileptonic channel of our top quark pairs. Although the W bosons can decay to any lepton, we did not consider the decays to τ leptons, since they decay into hadrons or into a less massive lepton and two neutrinos, making this channel more difficult to reconstruct. The events were generated by setting the transverse momentum (p_T) of jets above 20 GeV. Photons and leptons were required to have $p_T > 10$ GeV. No constraints were applied to the pseudorapidity at generation level. Figure 13 shows

some Feynman diagrams that contribute the most to the signal production at the LHC.

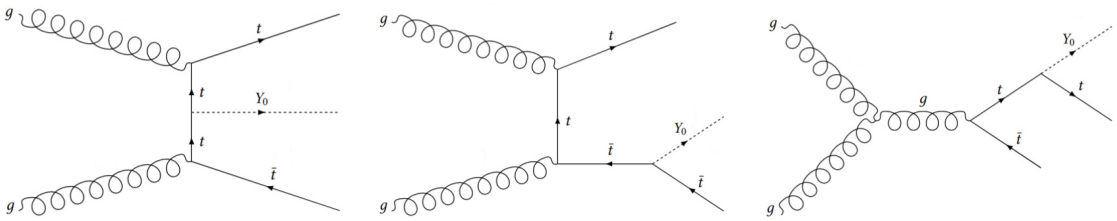

Figure 13: Feynman diagrams of $t\bar{t}Y_0$ production at LO.

Backgrounds from SM $t\bar{t}$ with up to 3 jets ($t\bar{t}$ + 3 jets), $t\bar{t}V$ with up to 1 jet ($V = W, Z$, $t\bar{t}V$+ jets), single top quark production (t-, s- and Wt-channels), $W(Z)$ with up to 4 jets (W/Z + 4 jets), $W/Zb\bar{b}$ with up to 2 jets ($W/Zb\bar{b}$ + 2 jets) and WW, ZZ, WZ diboson processes were also generated using `MadGraph5_aMC@NLO`, at LO. The $t\bar{t}b\bar{b}$ was generated at Next-to-Leading Order (NLO). All signal and background events are showed in Table 1 together with the corresponding generated number of events and cross-sections.

Table 1: Expected cross-sections, in pb, with basic generator selection cuts and including the decays of the top quark, the Higgs, $W^{\pm}$ and Z bosons at 13 TeV for the signal sample and some background events at the LHC.

Process	Order	Number of events generated	Obtained cross-section (pb)
$t\bar{t}Y_0$	LO	1000000	0.021
$t\bar{t}H$	NLO	2500000	0.023
$t\bar{t}b\bar{b}$	NLO	1600000	0.79
$t\bar{t}$ + 3 jets	LO	2000000	37.89
$t\bar{t}V$ + jets	LO	500000	0.062
Single top s-channel	LO	840000	2.19
Single top t-channel	LO	1040000	46.86
Single top Wt-channel	LO	1000000	15.18
W + 4 jets	LO	500000	34500.0
$Wb\bar{b}$ + 2 jets	LO	500000	289.0
Z + 4 jets	LO	500000	3120.0
$Zb\bar{b}$ + 2 jets	LO	500000	123.0
WW + 3 jets	LO	500000	84.2
WZ + 3 jets	LO	200000	37.9
ZZ +3 jets	LO	820000	11.0

The single top quark cross-sections were evaluated at NNLO in QCD for the $t-$channel [69, 70] and at NLO for the $Wt-$channel [71] and $s-$channel [72, 73]. For $t\bar{t}$ + 3 jets, its cross-section has been calculated at NNLO in QCD, including resummation of NNLL soft gluon terms using Top++2.0 [74] and is predicted to be 832^{+40}_{-46} pb for a top quark mass of 172.5 GeV.

3.2 DELPHES simulation parameters

Like previously mentioned, for the fast simulation of a general-purpose detector, Delphes was used, applying the default ATLAS parameter card. An outline of some of these parameters is given in this section.

Particle propagation is given in a cylinder with radius r = 1.15 m and length l = 3.51 m, under a magnetic field B_z = 2 T. The particle tracking efficiencies are defined as a function of $|\eta|$ and p_T, and separately for charged hadrons, electrons and muons. For values of $|\eta| > 2.5$ and $p_T \leq 0.1$ GeV all charged particle tracking efficiencies are zero and range between 70% to 75% for values in the range 0.1 GeV $< p_T <$ 1 GeV. For higher p_T values, $p_T > 1$ GeV, the tracking efficiency for charged hadrons lies between 85% (for $|\eta| \leq 2.5$) and 95% (for $|\eta| \leq 1.5$). For electrons it ranges from 83% to 99% and for muons is always larger than 98%. Momentum resolution for charged tracks is also defined as a function of η and p_T and it is never larger than 5%.

As mentioned before, the calorimeters are segmented in (η, ϕ) rectangular cells. For $|\eta| \leq 2.5$, the cells have dimensions (η, ϕ) = (0.1, 10°), and for $|\eta| > 2.5$, the cells have dimensions (η, ϕ) = (0.2, 20°). The ECAL and HCAL resolutions are defined as a function of energy, in a similar fashion as the energy resolution for electrons. For electrons, photons and π^0 mesons the energy deposition fractions are f_{ECAL} = 1 and f_{HCAL} = 0. For kaon and Λ particles these values were defined as f_{ECAL} = 0.3 and f_{HCAL} = 0.7. For any other long-lived particle, the values were set to f_{HCAL} = 1 and f_{ECAL} = 0. Finally, for muons and neutrinos, both energy fractions were set to zero.

The identification efficiencies for photons, electrons and muons are defined in segments of $|\eta|$ and are 95% in the region $|\eta| \leq 1.5$, 85% in the region $1.5 < |\eta| \leq 2.5$ (2.7 for muons) and 0% for $|\eta| > 2.5$ or for p_T values below 10 GeV. The parameters defined in section 2.3.4 for checking whether a particle is isolated or not, were set to p_T^{min} = 0.5 GeV, R = 0.5 and I_{min} = 0.1.

For the jet reconstruction, the anti-k_t jet clustering algorithm [75] was used. This algorithm iteratively clusters particles together based on their distances in the detector, using a distance metric that considers their p_T and the cone size parameter, or just distance, R. The algorithm then proceeds by identifying the pair of particles with the smallest distance. If the distance is smaller than a certain threshold defined by R, the two particles are merged together to form a single "proto-jet." If the distance is larger than R, the particle with the smallest distance is considered a "seed" and forms its own proto-jet. The algorithm then recalculates the distances between the proto-jets and particles, as well as between the proto-jets themselves. This process is repeated until all particles are assigned to a proto-jet. The resulting proto-jets represent the reconstructed jets in the event. One of the key features of this algorithm is its infrared and collinear safety. This means that the algorithm is less sensitive to the emission of soft and collinear particles, which can often occur in particle collisions. This property helps to mitigate the impact of experimental and theoretical uncertainties. In our analysis, the cone size R parameter was set to 0.6 and only jets with $p_T > 20$ GeV were allowed. A b-tagging efficiency is also implemented and is given separately for b-jets and c-jets, limited to 50% for b-jets and 20% for c-jets. It is zero for jets with $p_T \leq 10$ GeV or $|\eta| > 2.5$. To take into account possible misidentification, there is a default constant set to 0.2% to

simulate a misidentification rate.

3.3 Event selection and reconstruction

MadAnalysis5 [76], in the expert mode, was used for event analysis. It reads all the generated and simulated data and for each processed event it performs the necessary analysis and reconstruction, saving all variables for later use. For every event three levels of information are available for each of which the same set of variables is replicated. These levels are:

- the generator or parton level (labelled as GEN), which keeps the Monte Carlo (MC) information of every particle at generation;
- the reconstruction level with truth-match (labelled as REC), where jets and leptons are matched to generated particles;
- the experimental level or reconstruction without truth-matching, just like in a real experiment (labelled as EXP), where only jets and leptons are considered.

The output information from MadAnalysis5 is stored in ROOT format files.

At GEN level we have access to all MC information about the event: all particles are identifiable, including the ones that come from the decay chains of the heavier particles (top quarks and W bosons). At this level, it is possible to reconstruct the full decay chain of any particle by looking into the event history. Moreover, information about the full 4-momentum of each particle is also obtainable, including the experimentally undetected neutrinos and DM particles.

In the REC level, the jets and leptons after DELPHES simulation are matched, using a proximity criteria, to the parton level particles they most likely originated from. At this level, both the MC generator and simulated information, are used. This level is particularly interesting as it allows to check how well the kinematic reconstruction works, as described later, whenever the right jets and leptons corresponding to their parton level particles, are considered.

For the EXP level, only reconstructed jets and leptons are considered, just like in a real experiment, and no information at generator level is used whatsoever. Every quantity or observable reconstructed at this level only uses the information from jets and leptons as they were reconstructed in a real life experiment.

3.3.1 Event selection criteria

Events are pre-selected by requiring at least two jets and two opposite charge leptons in the final state, with pseudo-rapidities (η) below 2.5 and transverse momenta (p_T) above 20 GeV. Events are further selected by accepting the ones with two isolated leptons with opposite charges and invariant mass $m_{\ell^+\ell^-}$, outside a window of 10 GeV width, around the Z boson mass (m_Z = 91 GeV), to avoid contamination from the Z + jets background. Only events with exactly 2 $b-$jets are accepted.

3.3.2 Truth-match

The main purpose of performing truth-match is to match jets and leptons reconstructed by DELPHES i.e., the objects that are directly accessible in a real life experiment, to their parton level original particles, as mentioned above. We have only used signal events in the studies performed with truth-match, as is normally the case. The reconstructed leptons are matched to the generated ones, by requiring they lie inside a cone of $\Delta R < 0.1$ around the lepton at parton level. Among all detected leptons that may fulfill this condition, the closest reconstructed one to the particle at parton level, is considered the matched lepton. The same criteria is applied to the jets, but the matching cone was enlarged to $\Delta R < 0.4$. Following the event selection defined previously, only jets and leptons with $p_T > 20$ GeV, were used.

3.3.3 Pairing jets and leptons with TMVA

In a real life experiment there is no access to parton level information. In this case, it's not obvious how the jets detected experimentally can be paired to the right leptons, in order to reconstruct the W and top quark parents, they were originated from. Given the number of jets present in $t\bar{t}Y_0$ signal events, this may be a very hard task to accomplish. To overcome this difficulty, we used the distributions of ΔR, $\Delta\phi$ and $\Delta\theta$ between jets (j_1, j_2) and leptons (ℓ^+, ℓ^-), as well as the mass difference $[m(\ell^+, j_1) - m(\ell^-, j_2)]$, (Δm), in order to compute the highest probability of having the right pairing between jets and leptons. This is done even before trying to make the kinematic reconstruction of the $t\bar{t}Y_0$ events. In Figure 14, we show the distributions of ΔR, $\Delta\phi$, $\Delta\theta$ and Δm in blue, whenever we have the right pairing between the leptons and jets coming from the same top quark parents and in red, whenever the jets from the top quarks were swapped. As we can see, clear differences exist when we have the right and wrong pairings in all distributions. The distributions showed in Figure 14 were obtained at parton level. They were used by the TMVA [77], when looping over all possible jets and leptons combinations, to compute the highest probability of getting the right pairing combination. The exact list of variables used by TMVA (not shown here, once they are very much equivalent to the ones already showed) includes the ΔR, $\Delta\phi$ and $\Delta\theta$ of the following pairs: (b_t, l^+), (b_t, l^-), $(\bar{b_{\bar{t}}}, l^+)$ and $(\bar{b_{\bar{t}}}, l^-)$. The correlations among the variables used are shown in Figure 15 for the good, labelled as signal, and bad combinations, labelled as background. Several multivariate methods were compared and the BDTG gave the best performance in identifying the correct combination of jets and leptons, as can be confirmed through the ROC curve, represented in Figure 16 (left). The distribution of the BDTG classifier is shown in Figure 16 (right). It is clear from the ROC curve that is indeed possible to obtain the right combination of jets and leptons with very high probability.

3.3.4 Kinematic fit

Given the fact that TMVA was very much successful to pair the right jets to the right leptons, originated from the W bosons and top quarks, we have decided to apply a kinematic fit to signal events. In order to do so, we have assumed that all the transverse missing energy $(\not{E}^x, \not{E}^y)$, came from the undetected

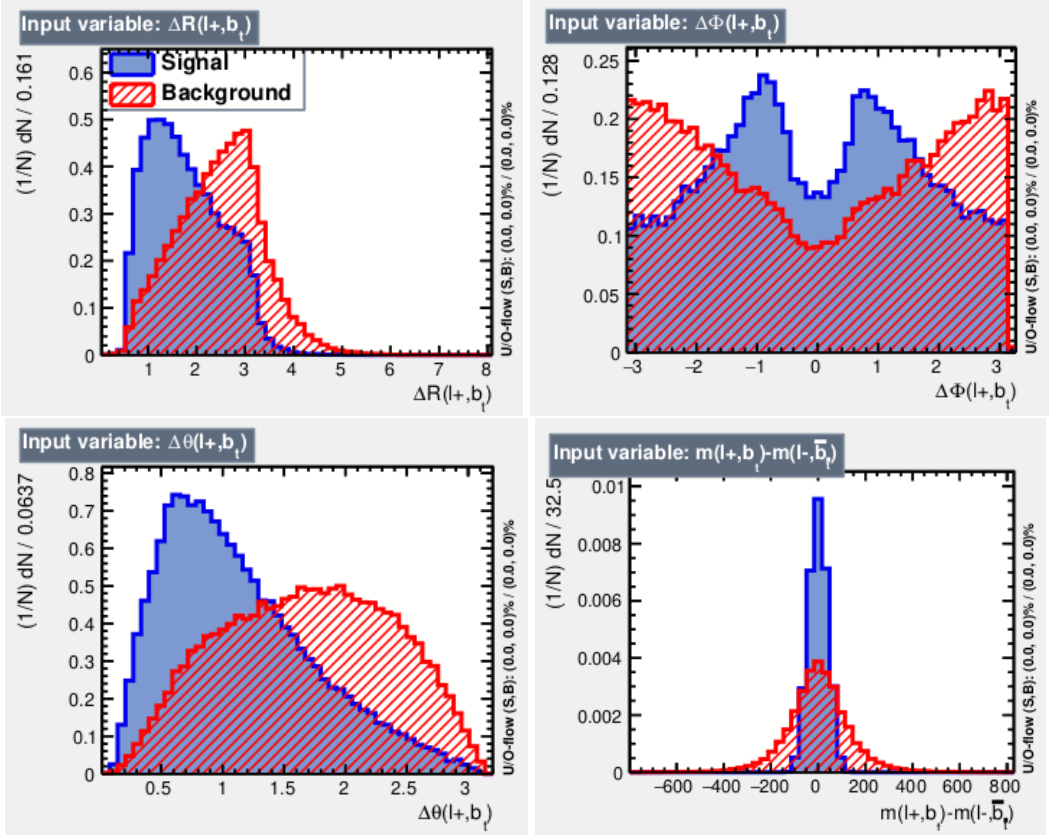

Figure 14: Normalized TMVA input variable distributions for correct combinations (labeled as *signal*, in blue) and wrong combinations (labeled as *background*, in red), as an example for a DM $J^P = 0^-$ mediator. The ΔR between the ℓ^+ and the b-jet from the t decay (top left); the corresponding $\Delta\phi$ distribution (top right); $\Delta\theta$ (bottom left); and Δm (bottom right), are shown.

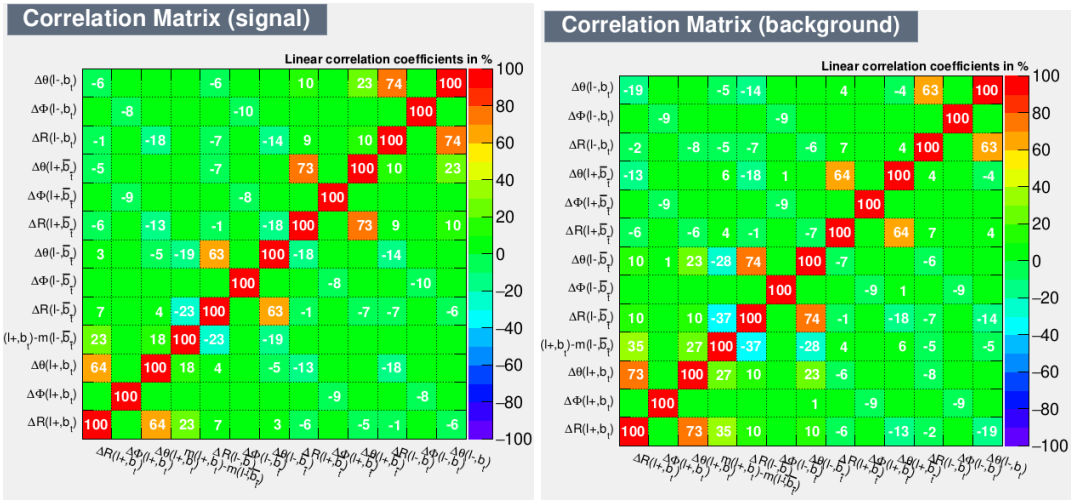

Figure 15: Matrix correlations between the TMVA input variables for the signal (left) and background (right) samples.

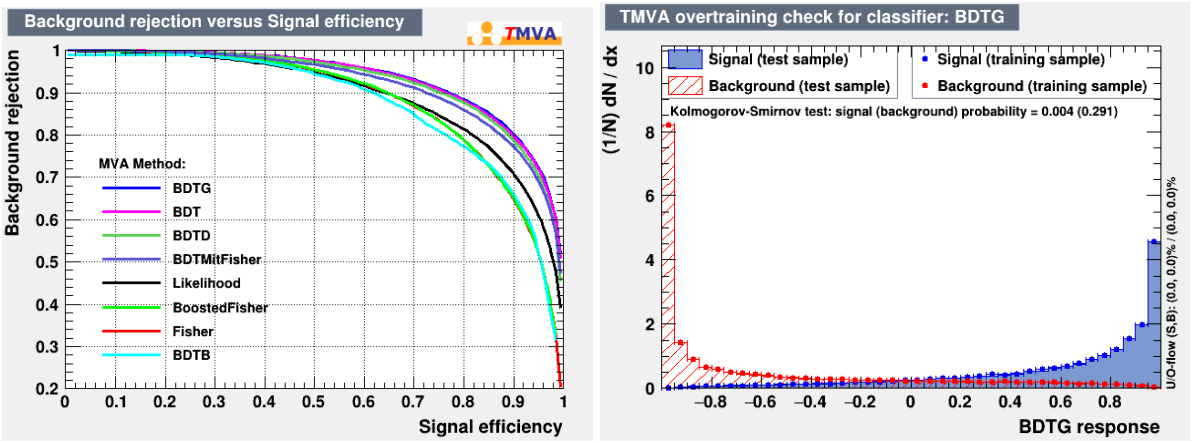

Figure 16: Background rejection versus signal acceptance (ROC curve) for different multivariate methods are compared, for the mediator (left). The distribution of the best classifier discriminant (BDTG) is also shown (right).

neutrinos i.e.,

$$p_{\nu}^{x} + p_{\bar{\nu}}^{x} = \not{E}^{x} \tag{3.1}$$

$$p_{\nu}^{y} + p_{\bar{\nu}}^{y} = \not{E}^{y} \quad , \tag{3.2}$$

where the values of each component of the missing energy are calculated using the sum of the p_T of all leptons and jets present in the event. In order to determine the components of the 4-momenta of the neutrino and anti-neutrino (six unknowns), we use 4-momentum conservation in the decay chain of the W bosons and top quarks. This implies that,

$$\begin{aligned}
(P_{\nu} + P_{\ell^+})^2 &= m_{W^+}^2 \\
(P_{\bar{\nu}} + P_{\ell^-})^2 &= m_{W^-}^2 \\
P_{W^+} &= P_{\ell^+} + P_{\nu} \\
P_{W^-} &= P_{\ell^-} + P_{\bar{\nu}} \\
(P_{W^+} + P_b)^2 &= m_t^2 \\
(P_{W^-} + P_{\bar{b}})^2 &= m_{\bar{t}}^2 \quad ,
\end{aligned} \tag{3.3}$$

where the masses of the W bosons ($m_{W^{\pm}}$) and the top-quarks ($m_{t,\bar{t}}$) are randomly generated from Two-dimensional Probability Density Function (2D PDF), constructed with parton level information. In equation 3.3, P_i ($i = \nu, \bar{\nu}, b, \bar{b}, \ell^+, \ell^-, W^{\pm}$) correspond to the 4-momentum of particles. Since we have a system of quadratic equations, there might be multiple solutions for the momenta of the neutrinos. If no solution is found, the mass generation is repeated up to a maximum of 500 times. The event is discarded if no solution has been found after these repetitions. In the case where we have multiple solutions, a likelihood function is calculated for each one from the transverse momenta 2D PDFs of the neutrinos, top-quarks and the $t\bar{t}$ system at generator level, respectively $P(p_{T_{\nu}})$, $P(p_{T_{\bar{\nu}}})$, $P(p_{T_t})$, $P(p_{T_{\bar{t}}})$ and $P(p_{T_{t\bar{t}}})$.

For this kinematic fit, the chosen solution among the set is the one that maximizes the likelihood

$$L \propto \frac{1}{p_{T_\nu} p_{T_{\bar{\nu}}}} P(p_{T_\nu}) P(p_{T_{\bar{\nu}}}) P(p_{T_t}) P(p_{T_{\bar{t}}}) P(p_{T_{t\bar{t}}}), \tag{3.4}$$

where the normalisation factor $1/p_{T_\nu} p_{T_{\bar{\nu}}}$ is applied in the likelihood to account for the energy losses due to the radiation emission and effects from the detector resolutions which will increase the reconstructed neutrino four-momentum.

Using REC objects (jets and leptons) i.e., when we are sure that the right jets and leptons match the correct parton level particles from the top quarks and W boson decays, the kinematic reconstruction efficiency obtained was 72%. A reconstruction efficiency of (nearly) 100% is not possible since jets, leptons and $\not{E}_T$, which are used in the kinematic fit, are already affected by the detector resolution and inefficiencies, as well as the limitations of the jet reconstruction algorithm implemented. Due to these effects, sometimes it's not simply possible to obtain a solution to the kinematic reconstruction. Nevertheless, a significant number of signal events are reconstructed supporting the decisions made, particularly in what concerns the $\not{E}_T$. Figure 17 shows 2-dimensional p_T distributions of the neutrino (top left), the top quark (top right), the $t\bar{t}$ system (bottom left) and the W^+ boson (bottom right), resulting from the truth-match reconstruction. The correlation between parton-level particles and the respective reconstructed ones (with truth-match) is clearly visible. In particular, we can clearly see that the $t\bar{t}$ system, very sensitive to the presence of the DM mediator, has its p_T quite well reconstructed.

Equivalent distributions were also produced using EXP objects (jets and leptons correctly assigned to the W boson and top quark decays using the TMVA tool), which confirmed that the reconstruction of the $t\bar{t}$ system in $t\bar{t}Y_0$ events is possible even when considering the $\not{E}_T$ approximation used. Figure 18 shows the 2-dimensional p_T distributions of the neutrino (top left), the top quark (top right), the $t\bar{t}$ system (bottom left) and the W^+ boson (bottom right), resulting from the kinematic reconstruction performed with EXP jets and leptons i.e., using the objects that usually are reconstructed in a real life experiment. Even though, as expected, the distributions are slightly broader, the correlation between parton-level particles and the respective reconstructed ones (without truth-match) is clearly visible, implying a good quality kinematic reconstruction of the $t\bar{t}$ system. The number of events after all selection cuts and the kinematic reconstruction are represented in Table 2.

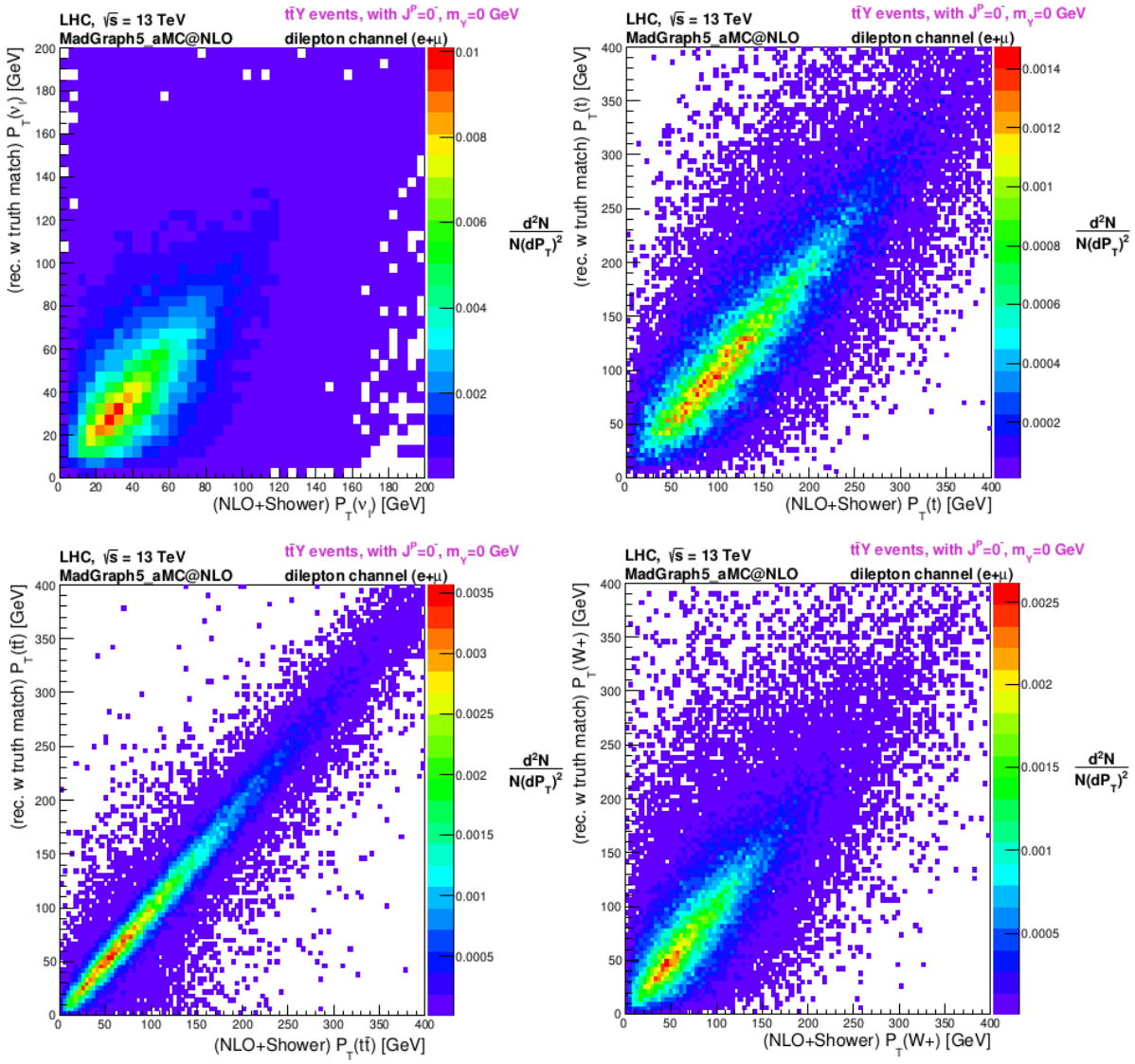

Figure 17: Two-Dimensional distributions in $t\bar{t}Y_0$ events: generator-level transverse momentum (GEN) versus reconstructed transverse momentum (with truth-match, REC) for the neutrino (top left), top quark (top right), $t\bar{t}$ system (bottom left) and W^+ boson (bottom right).

Table 2: Events after all selections applied for 100 fb^{-1}.

Process	Events		
$t\bar{t}Y_0$	103.4	±	0.6
$t\bar{t}H$	69.1	±	0.5
$t\bar{t}b\bar{b}$	1997.4	±	32.0
$t\bar{t}$ + 3 jets	59138.4	±	456.3
$t\bar{t}V$ + jets	96.8	±	2.2
Single top Wt-channel	1153.9	±	59.3
$Zb\bar{b}$ + 2 jets	560.8	±	211.9
ZZ +3 jets	10.2	±	7.2

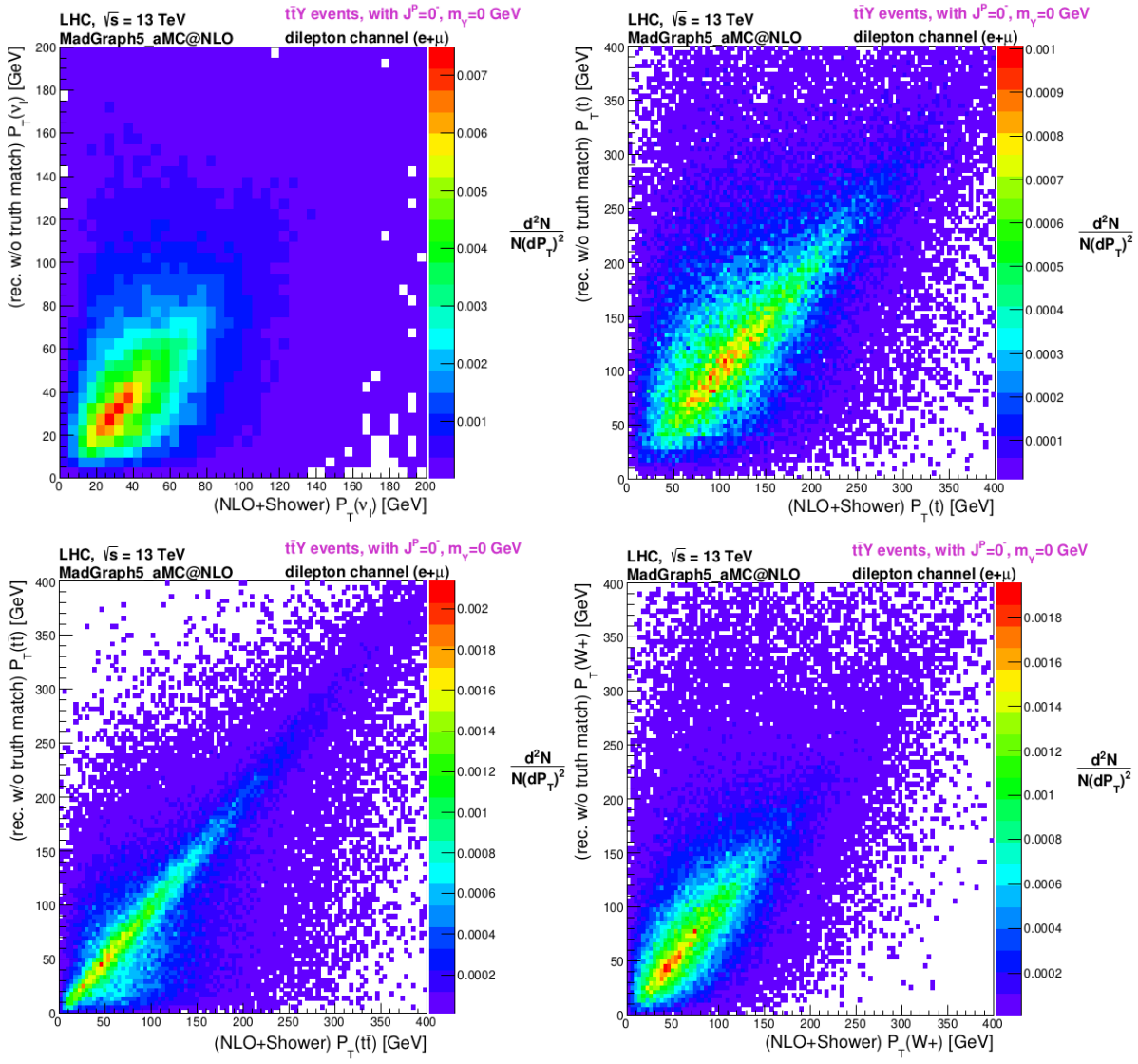

Figure 18: Two-Dimensional distributions in $t\bar{t}Y_0$ events: generator-level transverse momentum (GEN) versus experimental transverse momentum (without truth-match, EXP) for the neutrino (top left), top quark (top right), $t\bar{t}$ system (bottom left) and W^+ boson (bottom right).

4

Results and discussion

In this Chapter our main results are discussed. The angular distributions used are introduced with the goal of understanding if, at the LHC, the nature of the couplings of the DM mediator to the top quarks, can be probed. Exclusion limits on these couplings are presented, considering several hypothesis.

4.1 Angular distributions

Several CP-observables have been proposed and explored extensively to directly probe the CP-nature of the Yukawa top quark couplings at the LHC [78, 79]. The $t\bar{t}H$ production was used for this purpose. As the $t\bar{t}H$ final states are quite similar to the associated production of DM mediators with top quarks ($t\bar{t}Y_0$), we find interesting to explore if these same observables can be used in the study of $t\bar{t}Y_0$. We are particularly interested here in the low mass region of the DM mediators (m_{Y_0} = 0 GeV). As already observed in the $t\bar{t}H$ studies, we expect the observables to be sensitive to the scalar (CP-even) and pseudoscalar (CP-odd) nature of DM mediator. Particularly interesting is the case where the DM candidate is a mixed state where $g^S_{u_{33}}$ and g^P_{u33} may both be different from zero. As any mixed state can be reconstructed using an overlap of the pure scalar and pseudoscalar components, most of the angular distributions showed in this chapter only have represented these two extreme cases for the couplings. During the course of the studies performed for this thesis, where many observables were looked into, the difference of the azimuthal angle of the two leptons (originated in the top quarks decays), $\Delta\phi_{\ell^+\ell^-}$, and the b_4 variables were paradigmatic cases of good observables that could be used here. As it is not possible to reconstruct the full $t\bar{t}Y_0$ system (but only the $t\bar{t}$), the variables were evaluated in the Laboratory Frame (LAB). The b_4 variable is defined according to

$$b_4 = \frac{(p_t^z . p_{\bar{t}}^z)}{(|\vec{p}_t| . |\vec{p}_{\bar{t}}|)} \quad , \tag{4.1}$$

where $\vec{p}_t$ ($\vec{p}_{\bar{t}}$) is the 3-momentum of the top (anti-top) quark and p_t^z ($p_{\bar{t}}^z$) its z component, where the $z-$direction corresponds to the beam line, as usual. In Figure 19, the $\Delta\phi_{\ell^+\ell^-}$ and b_4 variables are represented for an integrated luminosity of 100 fb^{-1}, after event selection and full kinematic reconstruction of the $t\bar{t}$ system. The $\not{E}_T$ distribution is also shown for completeness. The pure scalar ($g^S_{u_{33}}$ = 1 and

$g^P_{u_{33}} = 0$) and pseudoscalar ($g^S_{u_{33}} = 0$ and $g^P_{u_{33}} = 1$) cases are shown with scaling factors of 2 and 500, respectively, for better visualization. For the b_4 variable we can see that, in the scalar case (in brown), events tend to populate positive values more than negative values of the distribution. This behaviour is inverted in the pseudoscalar case (in orange). Regarding the $\Delta\phi_{\ell^+\ell^-}$ distribution, a different behaviour can also be observed between the two cases. Although the distribution is symmetric in both cases, for the scalar, events are more evenly distributed, while for the pseudoscalar, events tend to be populated in the extreme regions of $\Delta\phi_{\ell^+\ell^-}$. For the $\not{E}_T$ distribution, the pseudoscalar case tend to show a slightly larger range of values.

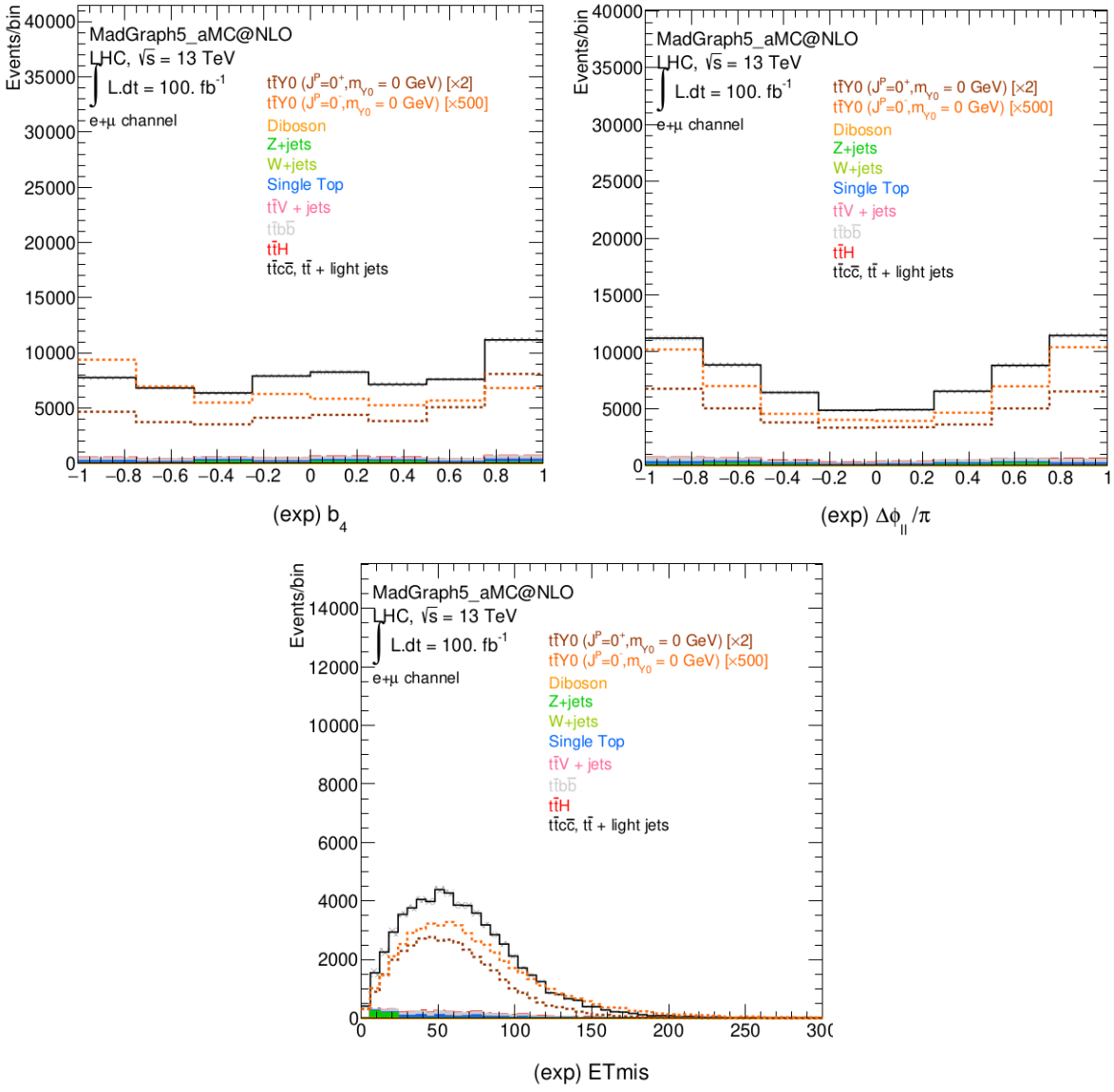

Figure 19: The b_4 (left), $\Delta\phi_{\ell^+\ell^-}$ (right) and missing E_T (bottom) for scalar and pseudo-scalar signals (dashed curves) together with the SM processes (full lines) with dileptonic final states, are represented after event selection and kinematic reconstruction, for a reference luminosity of 100 fb^{-1}. Scaling factors are applied to the scalar and pseudo-scalar signals for convenience.

4.2 Exclusion limits on DM mediator from SM

Exclusion CLs on the scalar and pseudoscalar nature of the top quark couplings to the DM mediator are set in two different scenarios, as a function of the LHC luminosity, up to the High-Luminosity phase of the LHC (HL-LHC). Two luminosities are considered i.e., L = 200 fb^{-1} and L = 3000 fb^{-1}. The two scenarios defined are the following:

- Scenario 1: exclusion of the SM plus a new CP-mixed DM mediator, assuming the SM. In this case, a null hypothesis is defined (H_0) as the SM only hypothesis, while a signal hypothesis is introduced (H_1) for the SM plus a CP-mixed signal;
- Scenario 2: exclusion of the SM plus a new CP-mixed DM mediator, assuming the SM plus a new CP-even DM mediator has already been discovered. In this scenario, H_0 is the SM plus the new CP-even signal, while H_1 is the SM plus a CP-mixed signal.

For each scenario under study, 100k pseudo experiments are generated for both the null and signal hypotheses, applying bin-by-bin Poisson fluctuations on the angular distributions used to calculate the exclusion limits ($\Delta\phi_{\ell^+\ell^-}$ and b_4). For each pseudo experiment, the probability that it is consistent with the null and signal hypothesis are computed (for both scenarios) and their ratio is used to define a test statistics, Q. We define the CL of the test-statistic as [80]

$$CL = P_{H_0}(Q \leq Q_{H_1}), \tag{4.2}$$

where Q_{H_1} is the median value of the test statistics of the signal hypothesis and P_{H_0} is the integrated probability of the test statistics of the null hypothesis, when $Q \leq Q_{H_1}$.

In Figures 20 and 21 the exclusion limits are shown for the $\Delta\phi_{\ell^+\ell^-}$ and b_4 observables, respectively, for an integrated luminosity corresponding roughly to the RUN 2 luminosity plus the contribution from the first year of RUN 3 i.e., L = 200 fb^{-1}. Results for the full luminosity expected at the end of the HL-LHC (L = 3000 fb^{-1}) are also shown. The CL limits are shown as contour plots in the $(g^S_{u_{33}}, g^P_{u_{33}})$ 2D plane. The resulting 68% and 95% exclusion limits, for both luminosity values, are represented in Table 3, for Scenario 1, and in Table 4, for Scenario 2, for the $\Delta\phi_{\ell^+\ell^-}$ observable. In Tables 5 and 6 we have the same results for the b_4 observable.

Table 3: Exclusion limits for the Y_0 CP-couplings to the top quarks for fixed luminosities of 200 fb^{-1} and 3000 fb^{-1} of the SM plus a CP-mixed DM mediator, assuming the SM as the null hypothesis. The limits are shown at confidence levels of 68% and 95%, for the $\Delta\phi_{l^+l^-}$ variable.

Exclusion Limits from $\Delta\phi_{l^+l^-}$		L = 200 fb^{-1} (68% CL)	L = 200 fb^{-1} (95% CL)	L = 3000 fb^{-1} (68% CL)	L = 3000 fb^{-1} (95% CL)
m_{Y_0} = 0 GeV	$g^S_{u_{33}} \in$	[-0.067, +0.067]	[-0.127, +0.127]	[-0.032, +0.032]	[-0.062, +0.062]
	$g^P_{u_{33}} \in$	[-0.91, +0.91]	[-1.71, +1.71]	[-0.44, +0.44]	[-0.85, +0.85]

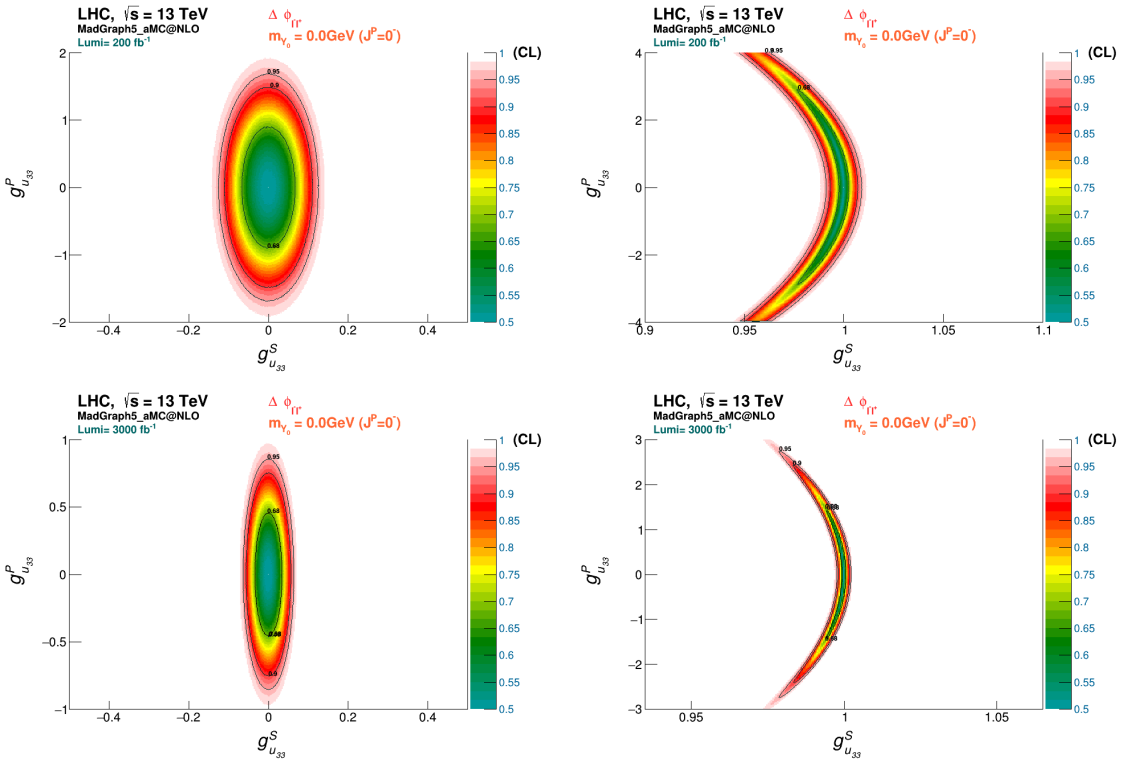

Figure 20: CLs for the exclusion of the SM with a massless DM mediator, Y_0, with mixed scalar and pseudo-scalar couplings, for scenario 1 (left) and scenario 2 (right), for the $\Delta\phi_{\ell^+\ell^-}$ between the charged leptons, for luminosities of 200 fb^{-1} and 3000 fb^{-1}.

Table 4: Exclusion limits for the Y_0 CP-couplings to the top quarks for fixed luminosities of 200 fb^{-1} and 3000 fb^{-1} of the SM plus a CP-mixed DM mediator, assuming the SM plus a CP-even particle as the null hypothesis. The limits are shown at confidence levels of 68% and 95%, for the $\Delta\phi_{l^+l^-}$ variable.

Exclusion Limits from $\Delta\phi_{l^+l^-}$		L = 200 fb^{-1} (68% CL)	L = 200 fb^{-1} (95% CL)	L = 3000 fb^{-1} (68% CL)	L = 3000 fb^{-1} (95% CL)
m_{Y_0} = 0 GeV	$g^S_{u33} \in$	[0.975, 1.003]	[0.947, 1.009]	[0.994, 1.001]	[0.978, 1.002]
	$g^P_{u33} \in$	[-2.94, 2.92]	[-4.02, 4.0]	[-1.48, 1.475]	[-2.785, +2.795]

Table 5: Exclusion limits for the Y_0 CP-couplings to the top quarks for fixed luminosities of 200 fb^{-1} and 3000 fb^{-1} of the SM plus a CP-mixed particle, assuming the SM as the null hypothesis. The limits are shown at confidence levels of 68% and 95%, for the b_4 variable.

Exclusion Limits from b_4		L = 200 fb^{-1} (68% CL)	L = 200 fb^{-1} (95% CL)	L = 3000 fb^{-1} (68% CL)	L = 3000 fb^{-1} (95% CL)
m_{Y_0} = 0 GeV	$g^S_{u33} \in$	[-0.067, 0.067]	[-0.125, 0.125]	[-0.032, 0.032]	[-0.062, 0.062]
	$g^P_{u33} \in$	[-0.9, 0.9]	[-1.69, 1.69]	[-0.455, 0.455]	[-0.86, 0.86]

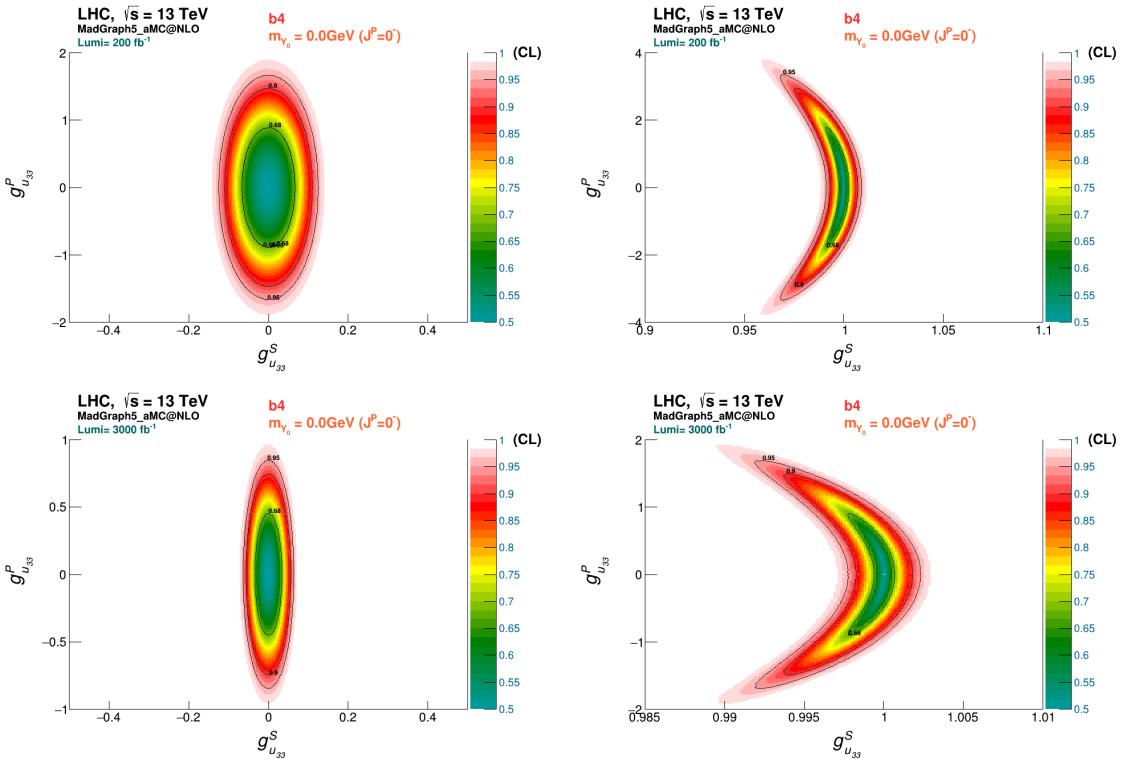

Figure 21: CLs for the exclusion of the SM with a massless DM mediator, Y_0, with mixed scalar and pseudo-scalar couplings, for scenario 1 (left) and scenario 2 (right), for the b_4 observable, for luminosities of 200 fb^{-1} and 3000 fb^{-1}.

Table 6: Exclusion limits for the Y_0 CP-couplings to the top quarks for fixed luminosities of 200 fb^{-1} and 3000 fb^{-1} of the SM plus a CP-mixed DM mediator, assuming the SM plus a new CP-even DM mediator as the null hypothesis. The limits are shown at confidence levels of 68% and 95%, for the b_4 variable.

Exclusion Limits from b_4		L = 200 fb^{-1} (68% CL)	L = 200 fb^{-1} (95% CL)	L = 3000 fb^{-1} (68% CL)	L = 3000 fb^{-1} (95% CL)
m_{Y_0} = 0 GeV	$g^S_{u_{33}} \in$	[0.991, 1.003]	[0.967, 1.009]	[0.998, 1.001]	[0.992, 1.002]
	$g^P_{u_{33}} \in$	[-2.94, 2.92]	[-4.02, 4.0]	[-0.895, 0.89]	[-1.72, 1.715]

For Scenario 1, the results obtained with b_4 and $\Delta\phi_{l^+l^-}$ are quite similar. It is interesting to realise that a significant portion of the $g^S_{u_{33}}$ and $g^P_{u_{33}}$ parameter space is possible to exclude already using 200 fb^{-1} with the simple analysis used in this thesis. When, however we consider Scenario 2 the b_4 variable evaluated in the LAB frame gives even better results than the $\Delta\phi_{l^+l^-}$ distributions, constraining more the pseudoscalar nature of the DM mediators couplings to the top quarks. Also, as expected, we can see a clear improvement on the exclusion limits as the luminosity increases.

5

Conclusions

Failing to provide a viable DM candidate, the SM needs extensions that can describe the mentioned astrophysical observations that imply the existence of this non-baryonic matter, accounting for approximately 27% of the mass of the Universe. The goal of the work presented in this thesis was, therefore, the exploration of a simplified DM model that works as a possible extension to the SM which allows the production of DM particles and mediators at the LHC at current center-of-mass energies.

In order to achieve this goal, a search for the production of DM mediators in association with a top quark pair ($t\bar{t}Y_0$) was performed, considering dileptonic final states of $t\bar{t}Y_0$ events. A new kinematic reconstruction method was developed for the $t\bar{t}$ system, which works even in the presence of a DM mediator that can't be detected. In this kinematic reconstruction, the missing transverse energy was fully attributed to the undetected neutrinos coming from the top quark decays. This approximation appears to be valid in the low mass regime of the DM mediator, in particular when m_{Y_0} = 0 GeV. The kinematic reconstruction efficiency of signal events was 72% confirming that the approximations used in the reconstruction were valid. Clear correlations among parton level objects and reconstructed objects were observed, justifying the approach used in the kinematic reconstruction.

We have analyzed several angular observables, for instance, the $\Delta\phi_{\ell^+\ell^-}$ and b_4 distributions, that were used to set CLs exclusion limits on the couplings of the proposed DM mediator to the top quarks, in two different scenarios. In Scenario 1 we considered the exclusion of the SM plus a new CP-mixed DM mediator, assuming the SM as the null hypothesis. In Scenario 2 the exclusion limits were evaluated for the SM plus a new CP-mixed DM mediator, assuming the SM plus a new CP-even DM mediator (with zero mass) has already been discovered. These studies were performed for a luminosity of 200 fb^{-1}, corresponding roughly to the full RUN 2 luminosity plus the contribution from the first year of RUN 3, and 3000 fb^{-1}, corresponding to the full luminosity expected at the end of the HL-LHC. For Scenario 1, the results obtained with b_4 are equivalent to the ones from $\Delta\phi_{l^+l^-}$. A significant coverage of the excluded $g^S_{u_{33}}$ and $g^P_{u_{33}}$ parameter space is observed already using 200 fb^{-1}. For Scenario 2 the results obtained with the b_4 variable, are better when compared with the ones obtained by $\Delta\phi_{l^+l^-}$. In particular, the pseudoscalar component of the DM mediator is better constrained using b_4. A clear improvement on the exclusion limits is observed as the luminosity increases. For Scenario 1, the best exclusion limits at 95%

CL are set to, $g^S_{u_{33}} \in [-0.062, 0.062]$ and $g^P_{u_{33}} \in [-0.86, 0.86]$. For Scenario 2, the best limits at 95% CL correspond to, $g^S_{u_{33}} \in [0.992, 1.002]$ and $g^P_{u_{33}} \in [-1.72, 1.715]$.

When compared to $t\bar{t}H$ searches, it is interesting to realise that the exclusion limits are set at more or less the same level, which motivates the search for this type of DM mediators in a real life experiment to be accomplished in the future. This, however, stays largely outside the scope of this thesis.

Bibliography

[1] J. M. Lourenço. *The NOVAthesis LaTeX Template User's Manual*. NOVA University Lisbon. 2021. url: https://github.com/joaomlourenco/novathesis/raw/master/template.pdf (cit. on p. ii).

[2] A. Einstein. "The foundation of the general theory of relativity." In: *Annalen Phys.* 49.7 (1916). Ed. by J.-P. Hsu and D. Fine, pp. 769–822. doi: 10.1002/andp.19163540702 (cit. on p. 1).

[3] B. Holstein. " The Theory of Almost Everything: The Standard Model, the Unsung Triumph of Modern Physics ". In: *Physics Today* 59.7 (2006-07), pp. 49–50. issn: 0031-9228. doi: 10.1063/1.2337829. url: https://doi.org/10.1063/1.2337829 (cit. on p. 1).

[4] S. L. Glashow. "Partial-symmetries of weak interactions". In: *Nuclear Physics* 22.4 (1961), pp. 579–588. issn: 0029-5582. doi: https://doi.org/10.1016/0029-5582(61)90469-2. url: https://www.sciencedirect.com/science/article/pii/0029558261904692 (cit. on p. 1).

[5] S. Weinberg. "A Model of Leptons". In: *Phys. Rev. Lett.* 19 (21 1967-11), pp. 1264–1266. doi: 10.1103/PhysRevLett.19.1264. url: https://link.aps.org/doi/10.1103/PhysRevLett.19.1264 (cit. on p. 1).

[6] A. Salam. "Weak and Electromagnetic Interactions". In: *Conf. Proc. C* 680519 (1968), pp. 367–377. doi: 10.1142/9789812795915_0034 (cit. on p. 1).

[7] J. Nieves, M. Valverde, and M. J. Vicente Vacas. "Charged and Neutral Current Neutrino Induced Nucleon Emission Reactions". In: *Acta Phys. Polon. B* 37 (2006). Ed. by K. M. Graczyk and J. T. Sobczyk, p. 2295. arXiv: hep-ph/0605221 (cit. on p. 1).

[8] J. Hansson. "Physical Origin of Elementary Particle Masses". In: *Electron. J. Theor. Phys.* 11.30 (2014), pp. 87–100. arXiv: 1402.7033 [physics.gen-ph] (cit. on p. 1).

[9] A. D. Sakharov. "Violation of CP Invariance, C asymmetry, and baryon asymmetry of the universe". In: *Pisma Zh. Eksp. Teor. Fiz.* 5 (1967), pp. 32–35. doi: 10.1070/PU1991v034n05ABEH002497 (cit. on p. 1).

[10] Y. Fukuda et al. “Evidence for oscillation of atmospheric neutrinos”. In: *Phys. Rev. Lett.* 81 (1998), pp. 1562–1567. doi: 10.1103/PhysRevLett.81.1562. arXiv: hep-ex/9807003 (cit. on p. 1).

[11] L. A. Mikaelyan and V. V. Sinev. “Neutrino oscillations at reactors: What next?” In: *Phys. Atom. Nucl.* 63 (2000). Ed. by V. A. Bednyakov, V. B. Brudanin, and S. G. Kovalenko, pp. 1002–1006. doi: 10.1134/1.855739. arXiv: hep-ex/9908047 (cit. on p. 1).

[12] K. Abe et al. “Evidence of Electron Neutrino Appearance in a Muon Neutrino Beam”. In: *Phys. Rev. D* 88.3 (2013), p. 032002. doi: 10.1103/PhysRevD.88.032002. arXiv: 1304.0841 [hep-ex] (cit. on p. 1).

[13] B. C. Barish and R. Weiss. “LIGO and the Detection of Gravitational Waves”. In: *Physics Today* 52.10 (1999-10), pp. 44–50. issn: 0031-9228. doi: 10.1063/1.882861. url: https://doi.org/10.1063/1.882861 (cit. on p. 2).

[14] J. C. Bustillo et al. “GW190521 as a Merger of Proca Stars: A Potential New Vector Boson of 8.7×10^{-13} eV”. In: *Phys. Rev. Lett.* 126 (8 2021-02), p. 081101. doi: 10.1103/PhysRevLett.126.081101. url: https://link.aps.org/doi/10.1103/PhysRevLett.126.081101 (cit. on p. 2).

[15] M. Backović et al. “Higher-order QCD predictions for dark matter production at the LHC in simplified models with s-channel mediators”. In: *Eur. Phys. J. C* 75.10 (2015), p. 482. doi: 10.1140/epjc/s10052-015-3700-6. arXiv: 1508.05327 [hep-ph] (cit. on pp. 2, 15, 34).

[16] L. Evans and P. Bryant. “LHC Machine”. In: *Journal of Instrumentation* 3.08 (2008-08), S08001. doi: 10.1088/1748-0221/3/08/S08001. url: https://dx.doi.org/10.1088/1748-0221/3/08/S08001 (cit. on p. 2).

[17] “The ATLAS Experiment at the CERN Large Hadron Collider”. In: *Journal of Instrumentation* 3.08 (2008-08), S08003. doi: 10.1088/1748-0221/3/08/S08003. url: https://dx.doi.org/10.1088/1748-0221/3/08/S08003 (cit. on p. 2).

[18] J. de Favereau et al. “DELPHES 3, A modular framework for fast simulation of a generic collider experiment”. In: *JHEP* 02 (2014), p. 057. doi: 10.1007/JHEP02(2014)057. arXiv: 1307.6346 [hep-ex] (cit. on pp. 2, 30).

[19] https://upload.wikimedia.org/wikipedia/commons/0/00/Standard_Model_of_Elementary_Particles.svg (cit. on p. 4).

[20] M. E. Peskin and D. V. Schroeder. *An Introduction to quantum field theory*. Reading, USA: Addison-Wesley, 1995. isbn: 978-0-201-50397-5 (cit. on p. 6).

[21] M. Kobayashi and T. Maskawa. “CP-Violation in the Renormalizable Theory of Weak Interaction”. In: *Progress of Theoretical Physics* 49.2 (1973-02), pp. 652–657. issn: 0033-068X. doi: 10.1143/PTP.49.652. url: https://doi.org/10.1143/PTP.49.652 (cit. on p. 8).

[22] "Observation of Top Quark Production in $\overline{p}p$ Collisions with the Collider Detector at Fermilab". In: *Phys. Rev. Lett.* 74 (14 1995-04), pp. 2626–2631. doi: 10.1103/PhysRevLett.74.2626. url: https://link.aps.org/doi/10.1103/PhysRevLett.74.2626 (cit. on p. 8).

[23] "Observation of the Top Quark". In: *Phys. Rev. Lett.* 74 (14 1995-04), pp. 2632–2637. doi: 10.1103/PhysRevLett.74.2632. url: https://link.aps.org/doi/10.1103/PhysRevLett.74.2632 (cit. on p. 8).

[24] R. L. Workman et al. "Review of Particle Physics". In: *PTEP* 2022 (2022), p. 083C01. doi: 10.1093/ptep/ptac097 (cit. on pp. 8, 9).

[25] *A profile likelihood approach to measure the top quark mass in the lepton+jets channel at* $\sqrt{s}$ = 13 TeV. Tech. rep. Geneva: CERN, 2022. url: https://cds.cern.ch/record/2806509 (cit. on p. 8).

[26] "Measurement of the top-quark mass using a leptonic invariant mass in pp collisions at $\sqrt{s}$ = 13 TeV with the ATLAS detector". In: (2022-09). arXiv: 2209.00583 [hep-ex] (cit. on p. 8).

[27] https://twiki.cern.ch/twiki/bin/view/LHCPhysics/LHCTopWGSummaryPlots (cit. on p. 8).

[28] "Measurement of Spin Correlation in Top-Antitop Quark Events and Search for Top Squark Pair Production in pp Collisions at $\sqrt{s}$ = 8 TeV Using the ATLAS Detector". In: *Phys. Rev. Lett.* 114 (14 2015-04), p. 142001. doi: 10.1103/PhysRevLett.114.142001. url: https://link.aps.org/doi/10.1103/PhysRevLett.114.142001 (cit. on p. 9).

[29] W. Kelvin. *Baltimore Lectures on Molecular Dynamics and the Wave Theory of Light*. C.J. Clay and Sons, 1904. url: https://archive.org/details/baltimorelecture00kelviala/mode/2up (cit. on p. 10).

[30] H. Poincaré. "The Milky Way and the theory of gases". In: *Popular Astronomy* 14 (1906), pp. 475–488 (cit. on p. 10).

[31] K. Lundmark. "Über die Bestimmung der Entfernungen, Dimensionen, Massen und Dichtigkeit fur die nächstgelegenen anagalacktischen Sternsysteme." In: *Meddelanden fran Lunds Astronomiska Observatorium Serie I* 125 (1930-01), pp. 1–13 (cit. on p. 10).

[32] F. Zwicky. "Die Rotverschiebung von extragalaktischen Nebeln". In: *Helvetica Physica Acta* 6 (1933-01), pp. 110–127 (cit. on p. 10).

[33] F. Zwicky. "On the Masses of Nebulae and of Clusters of Nebulae". In: 86 (1937-10), p. 217. doi: 10.1086/143864 (cit. on p. 10).

[34] H. W. Babcock. "The rotation of the Andromeda Nebula". In: *Lick Observatory Bulletin* 498 (1939-01), pp. 41–51. doi: 10.5479/ADS/bib/1939LicOB.19.41B (cit. on p. 10).

[35] M. S. Roberts and A. H. Rots. "Comparison of Rotation Curves of Different Galaxy Types". In: 26 (1973-08), pp. 483–485 (cit. on p. 11).

[36] R. A. Sunyaev. “The thermal history of the universe and the spectrum of relic radiation.” In: *Confrontation of Cosmological Theories with Observational Data*. Ed. by M. S. Longair. Vol. 63. 1974-01, pp. 167–173 (cit. on p. 11).

[37] D. Walsh, R. F. Carswell, and R. J. Weymann. “0957+561 A, B: twin quasistellar objects or gravitational lens?” In: 279 (1979-05), pp. 381–384. doi: 10.1038/279381a0 (cit. on p. 12).

[38] J. Wambsganss. “Gravitational lensing in astronomy”. In: *Living Rev. Rel.* 1 (1998), p. 12. doi: 10.12942/lrr-1998-12. arXiv: astro-ph/9812021 (cit. on p. 12).

[39] X.-P. Wu. “Gravitational lensing in the universe”. In: *Fund. Cosmic Phys.* 17 (1996), p. 1. arXiv: astro-ph/9512110 (cit. on p. 12).

[40] S. Liebes. “Gravitational Lenses”. In: *Phys. Rev.* 133 (3B 1964-02), B835–B844. doi: 10.1103/PhysRev.133.B835. url: https://link.aps.org/doi/10.1103/PhysRev.133.B835 (cit. on p. 12).

[41] C. J. Copi, D. N. Schramm, and M. S. Turner. “Big bang nucleosynthesis and the baryon density of the universe”. In: *Science* 267 (1995), pp. 192–199. doi: 10.1126/science.7809624. arXiv: astro-ph/9407006 (cit. on p. 12).

[42] L. Bergström. “Nonbaryonic dark matter: Observational evidence and detection methods”. In: *Rept. Prog. Phys.* 63 (2000), p. 793. doi: 10.1088/0034-4885/63/5/2r3. arXiv: hep-ph/0002126 (cit. on p. 12).

[43] G. Hinshaw et al. “Five-Year Wilkinson Microwave Anisotropy Probe (WMAP) Observations: Data Processing, Sky Maps, and Basic Results”. In: *Astrophys. J. Suppl.* 180 (2009), pp. 225–245. doi: 10.1088/0067-0049/180/2/225. arXiv: 0803.0732 [astro-ph] (cit. on p. 12).

[44] W. Hu and M. J. White. “Acoustic signatures in the cosmic microwave background”. In: *Astrophys. J.* 471 (1996), pp. 30–51. doi: 10.1086/177951. arXiv: astro-ph/9602019 (cit. on p. 12).

[45] M. Milgrom. “A modification of the Newtonian dynamics as a possible alternative to the hidden mass hypothesis.” In: 270 (1983-07), pp. 365–370. doi: 10.1086/161130 (cit. on pp. 12, 14).

[46] K. Croswell. *The Universe at Midnight: Observations Illuminating the Cosmos*. Free Press, 2002. isbn: 9780743218818. url: https://books.google.pt/books?id=41XBXCJrPVwC (cit. on p. 12).

[47] P. Tisserand et al. “Limits on the Macho Content of the Galactic Halo from the EROS-2 Survey of the Magellanic Clouds”. In: *Astron. Astrophys.* 469 (2007), pp. 387–404. doi: 10.1051/0004-6361:20066017. arXiv: astro-ph/0607207 (cit. on p. 12).

[48] D. Clowe et al. “A direct empirical proof of the existence of dark matter”. In: *Astrophys. J. Lett.* 648 (2006), pp. L109–L113. doi: 10.1086/508162. arXiv: astro-ph/0608407 (cit. on p. 13).

[49] J. D. Bekenstein. "Relativistic gravitation theory for the MOND paradigm". In: *Phys. Rev. D* 70 (2004). [Erratum: Phys.Rev.D 71, 069901 (2005)], p. 083509. doi: 10.1103/PhysRevD.70.083509. arXiv: astro-ph/0403694 (cit. on p. 14).

[50] H. A. Buchdahl. "Non-linear Lagrangians and cosmological theory". In: 150 (1970-01), p. 1. doi: 10.1093/mnras/150.1.1 (cit. on p. 14).

[51] T. Padmanabhan. "Thermodynamical Aspects of Gravity: New insights". In: *Rept. Prog. Phys.* 73 (2010), p. 046901. doi: 10.1088/0034-4885/73/4/046901. arXiv: 0911.5004 [gr-qc] (cit. on p. 14).

[52] M. M. Brouwer et al. "First test of Verlinde's theory of Emergent Gravity using Weak Gravitational Lensing measurements". In: *Mon. Not. Roy. Astron. Soc.* 466.3 (2017), pp. 2547–2559. doi: 10.1093/mnras/stw3192. arXiv: 1612.03034 [astro-ph.CO] (cit. on p. 14).

[53] K.-H. Chae et al. "Testing the Strong Equivalence Principle: Detection of the External Field Effect in Rotationally Supported Galaxies". In: *Astrophys. J.* 904.1 (2020). [Erratum: Astrophys.J. 910, 81 (2021)], p. 51. doi: 10.3847/1538-4357/abbb96. arXiv: 2009.11525 [astro-ph.GA] (cit. on p. 14).

[54] R. D. Peccei. "The Strong CP problem and axions". In: *Lect. Notes Phys.* 741 (2008). Ed. by M. Kuster, G. Raffelt, and B. Beltran, pp. 3–17. doi: 10.1007/978-3-540-73518-2_1. arXiv: hep-ph/0607268 (cit. on p. 14).

[55] K. Garrett and G. Duda. "Dark Matter: A Primer". In: *Adv. Astron.* 2011 (2011), p. 968283. doi: 10.1155/2011/968283. arXiv: 1006.2483 [hep-ph] (cit. on p. 14).

[56] F. Ferrer, L. M. Krauss, and S. Profumo. "Indirect detection of light neutralino dark matter in the NMSSM". In: *Phys. Rev. D* 74 (2006), p. 115007. doi: 10.1103/PhysRevD.74.115007. arXiv: hep-ph/0609257 (cit. on p. 15).

[57] S.-H. Oh et al. "High-resolution mass models of dwarf galaxies from LITTLE THINGS". In: *Astron. J.* 149 (2015), p. 180. doi: 10.1088/0004-6256/149/6/180. arXiv: 1502.01281 [astro-ph.GA] (cit. on p. 15).

[58] W. Hu, R. Barkana, and A. Gruzinov. "Cold and fuzzy dark matter". In: *Phys. Rev. Lett.* 85 (2000), pp. 1158–1161. doi: 10.1103/PhysRevLett.85.1158. arXiv: astro-ph/0003365 (cit. on p. 15).

[59] A. M. Green and B. J. Kavanagh. "Primordial Black Holes as a dark matter candidate". In: *J. Phys. G* 48.4 (2021), p. 043001. doi: 10.1088/1361-6471/abc534. arXiv: 2007.10722 [astro-ph.CO] (cit. on p. 15).

[60] M. R. Buckley, D. Feld, and D. Goncalves. "Scalar Simplified Models for Dark Matter". In: *Phys. Rev. D* 91 (2015), p. 015017. doi: 10.1103/PhysRevD.91.015017. arXiv: 1410.6497 [hep-ph] (cit. on p. 15).

[61] J. Alwall, P. Schuster, and N. Toro. "Simplified Models for a First Characterization of New Physics at the LHC". In: *Phys. Rev. D* 79 (2009), p. 075020. doi: 10.1103/PhysRevD.79.075020. arXiv: 0810.3921 [hep-ph] (cit. on p. 15).

[62] D. Alves. "Simplified Models for LHC New Physics Searches". In: *J. Phys. G* 39 (2012). Ed. by N. Arkani-Hamed et al., p. 105005. doi: 10.1088/0954-3899/39/10/105005. arXiv: 1105.2838 [hep-ph] (cit. on p. 15).

[63] L. Fabbri. "LUCID: The ATLAS Luminosity Detector". In: *PoS* LHCP2018 (2018), p. 032. doi: 10.22323/1.321.0032 (cit. on p. 25).

[64] G. Aad et al. "Expected Performance of the ATLAS Experiment - Detector, Trigger and Physics". In: (2009-01). arXiv: 0901.0512 [hep-ex] (cit. on p. 29).

[65] M. Cacciari, G. P. Salam, and G. Soyez. "FastJet User Manual". In: *Eur. Phys. J. C* 72 (2012), p. 1896. doi: 10.1140/epjc/s10052-012-1896-2. arXiv: 1111.6097 [hep-ph] (cit. on p. 32).

[66] J. Alwall et al. "MadGraph 5 : Going Beyond". In: *JHEP* 06 (2011), p. 128. doi: 10.1007/JHEP06(2011)128. arXiv: 1106.0522 [hep-ph] (cit. on p. 34).

[67] P. Artoisenet et al. "Automatic spin-entangled decays of heavy resonances in Monte Carlo simulations". In: *JHEP* 03 (2013), p. 015. doi: 10.1007/JHEP03(2013)015. arXiv: 1212.3460 [hep-ph] (cit. on p. 34).

[68] T. Sjostrand, S. Mrenna, and P. Z. Skands. "PYTHIA 6.4 Physics and Manual". In: *JHEP* 05 (2006), p. 026. doi: 10.1088/1126-6708/2006/05/026. arXiv: hep-ph/0603175 (cit. on p. 34).

[69] J. Campbell, T. Neumann, and Z. Sullivan. "Single-top-quark production in the t-channel at NNLO". In: *JHEP* 02 (2021), p. 040. doi: 10.1007/JHEP02(2021)040. arXiv: 2012.01574 [hep-ph] (cit. on p. 35).

[70] R. D. Ball et al. "The PDF4LHC21 combination of global PDF fits for the LHC Run III". In: *J. Phys. G* 49.8 (2022), p. 080501. doi: 10.1088/1361-6471/ac7216. arXiv: 2203.05506 [hep-ph] (cit. on p. 35).

[71] N. Kidonakis and N. Yamanaka. "Higher-order corrections for tW production at high-energy hadron colliders". In: *JHEP* 05 (2021), p. 278. doi: 10.1007/JHEP05(2021)278. arXiv: 2102.11300 [hep-ph] (cit. on p. 35).

[72] P. Kant et al. "HatHor for single top-quark production: Updated predictions and uncertainty estimates for single top-quark production in hadronic collisions". In: *Comput. Phys. Commun.* 191 (2015), pp. 74–89. doi: 10.1016/j.cpc.2015.02.001. arXiv: 1406.4403 [hep-ph] (cit. on p. 35).

[73] M. Aliev et al. “HATHOR: HAdronic Top and Heavy quarks crOss section calculatoR”. In: *Comput. Phys. Commun.* 182 (2011), pp. 1034–1046. doi: 10.1016/j.cpc.2010.12.040. arXiv: 1007.1327 [hep-ph] (cit. on p. 35).

[74] M. Czakon and A. Mitov. “Top++: A Program for the Calculation of the Top-Pair Cross-Section at Hadron Colliders”. In: *Comput. Phys. Commun.* 185 (2014), p. 2930. doi: 10.1016/j.cpc.2014.06.021. arXiv: 1112.5675 [hep-ph] (cit. on p. 35).

[75] M. Cacciari, G. P. Salam, and G. Soyez. “The anti-kt jet clustering algorithm”. In: *Journal of High Energy Physics* 2008.04 (2008-04), p. 063. doi: 10.1088/1126-6708/2008/04/063. url: https://dx.doi.org/10.1088/1126-6708/2008/04/063 (cit. on p. 36).

[76] E. Conte, B. Fuks, and G. Serret. “MadAnalysis 5, A User-Friendly Framework for Collider Phenomenology”. In: *Comput. Phys. Commun.* 184 (2013), pp. 222–256. doi: 10.1016/j.cpc.2012.09.009. arXiv: 1206.1599 [hep-ph] (cit. on p. 37).

[77] A. Hoecker et al. “TMVA - Toolkit for Multivariate Data Analysis”. In: *arXiv e-prints*, physics/0703039 (2007-03), physics/0703039. doi: 10.48550/arXiv.physics/0703039. arXiv: physics/0703039 [physics.data-an] (cit. on p. 38).

[78] F. Boudjema et al. “Lab-frame observables for probing the top-Higgs interaction”. In: *Phys. Rev. D* 92.1 (2015), p. 015019. doi: 10.1103/PhysRevD.92.015019. arXiv: 1501.03157 [hep-ph] (cit. on p. 44).

[79] J. F. Gunion and X.-G. He. “Determining the CP nature of a neutral Higgs boson at the LHC”. In: *Phys. Rev. Lett.* 76 (1996), pp. 4468–4471. doi: 10.1103/PhysRevLett.76.4468. arXiv: hep-ph/9602226 (cit. on p. 44).

[80] A. L. Read. “Presentation of search results: The CL(s) technique”. In: *J. Phys. G* 28 (2002). Ed. by M. R. Whalley and L. Lyons, pp. 2693–2704. doi: 10.1088/0954-3899/28/10/313 (cit. on p. 46).